THE PLANT CELL

Membrane nanodomains modulate formin condensation for actin remodeling in Arabidopsis innate immune responses

Zhiming Ma [iD],[1] Yanbiao Sun [iD],[2] Xinlu Zhu [iD],[1] Liang Yang [iD],[1,3,4] Xu Chen [iD][2] and Yansong Miao [iD][1,*,†]

1 School of Biological Sciences, Nanyang Technological University, Singapore 637551, Singapore
2 Haixia Institute of Science and Technology, Horticultural Plant Biology and Metabolomics Centre, Fujian Agriculture and Forestry University, Fuzhou 350002, China
3 Singapore Centre for Environmental Life Sciences Engineering, Nanyang Technological University, Singapore 637551, Singapore
4 School of Medicine, Southern University of Science and Technology, 1088 Xueyuan Blvd, Nanshan District, Shenzhen, 518055, China

*Author for correspondence: yansongm@ntu.edu.sg
†Senior author.

Abstract

The assembly of macromolecules on the plasma membrane concentrates cell surface biomolecules into nanometer- to micrometer-scale clusters (nano- or microdomains) that help the cell initiate or respond to signals. In plant–microbe interactions, the actin cytoskeleton undergoes rapid remodeling during pathogen-associated molecular pattern-triggered immunity (PTI). The nanoclustering of formin-actin nucleator proteins at the cell surface has been identified as underlying actin nucleation during plant innate immune responses. Here, we show that the condensation of nanodomain constituents and the self-assembly of remorin proteins enables this mechanism of controlling formin condensation and activity during innate immunity in *Arabidopsis thaliana*. Through intrinsically disordered region-mediated remorin oligomerization and formin interaction, remorin gradually recruits and condenses formins upon PTI activation in lipid bilayers, consequently increasing actin nucleation in a time-dependent manner postinfection. Such nanodomain- and remorin-mediated regulation of plant surface biomolecules is expected to be a general feature of plant innate immune responses that creates spatially separated biochemical compartments and fine tunes membrane physicochemical properties for transduction of immune signals in the host.

Introduction

The plant actin cytoskeleton (AC) undergoes rapid reorganization during pattern-triggered immunity (PTI) responses (Staiger et al., 2009; Mostowy and Shenoy, 2015; Li and Staiger, 2018). During initial plant–microbe interactions, pathogen- or microbe-associated molecular patterns (PAMPs or MAMPs) trigger a rapid increase in host actin polymerization to coordinate cellular processes in defense mechanisms (Henty-Ridilla et al., 2013). Several actin-binding proteins, such as actin-depolymerizing factor (Henty-Ridilla et al.,

IN A NUTSHELL

Background: When bacterial pathogens attack a plant, the actin cytoskeleton in the plant host undergoes rapid remodeling to coordinate a series of host immune responses. Plasma membrane-localized formins act as the molecular switch for actin cytoskeleton polymerization in plant innate immune signaling. Our earlier studies revealed that bacteria-triggered plant innate immunity induces the macromolecular condensation of formin proteins into nanometer-scaled clusters on the plant cell surface that activate formin activities in actin polymerization. However, the underlying molecular mechanism by which pathogen infection induces formins to cluster in cell surface nanoclusters remains elusive.

Question: We wanted to identify the essential biomolecules that drive the condensation of formin proteins and activation of actin polymerization on the cell surface upon bacterial infection. Because plant class I formins on the cell surface are different from their mammalian homologs that are activated by GTPase, we explored other biophysical cues on the plant plasma membrane that modulate formin behavior and its activities in actin remodeling.

Findings: We found that bacterial infection triggers the clustering (condensation) of plant class I formins, which is dependent on plasma membrane compartmentalization—the formation of nanodomains. The molecular clustering of remorin proteins, the nanodomain assembly factor, on the plant cell surface was enhanced gradually at the early stages of bacterial infection. We were surprised to see similar spatiotemporal regulation in molecular clustering of the actin nucleator formin and the nanodomain resident protein remorin on the cell surface. Via different quantitative characterizations, we eventually deciphered the interaction model of formin and remorin on the membrane through artificial-lipid-bilayer-assisted *in vitro* reconstitution and *in vivo* advanced cell biology imaging. We further reconstituted the activation of actin remodeling upon the macromolecular condensation of remorin that recruits, clusters, and thereby activates formin proteins for actin polymerization.

Next steps: We are working towards a holistic view of fundamental principles by which surface nanodomains are assembled to activate or inactivate defense-relevant biomolecules and thereby their respective biochemical activities during host–pathogen interactions.

2014), capping protein (Li et al., 2015), and profilin (Sun et al., 2018b), are involved in PTI-triggered actin assembly.

Plant nucleator type-I formins were recently identified as molecular switches that activate *Arabidopsis thaliana* (Arabidopsis hereafter) actin polymerization upon PAMP elicitation, which depends on the clustering of formin proteins on the plasma membrane (PM; Ma et al., 2021). Plant type-I formins have been classified according to their conserved formin homology-2 (FH2) and FH1 domains and their additional N-terminal extracellular region and transmembrane domain, which anchor formin to the cell wall (CW) and PM, respectively (Deeks et al., 2002; Martiniere et al., 2011). Therefore, the molecular dynamics, nanoclustering, and biochemical activities of plant type-I formin could be fine tuned by changing the molecular composition or structure of any layer of the interconnected tensegrity structure formed by the CW–PM–AC continuum.

A recent study of actin remodeling during plant–bacteria communication revealed that host cellulose remodeling mediated by a bacterial quorum-sensing molecule, diffusible signal factor, could directly influence the molecular dynamics and activities of type-I formins in vivo. The increase in cellulose production mediated by diffusible signal factor increased the lateral motility of type-I formins through CW binding, which attenuated formin–formin interactions, thereby resulting in reduced oligomerization of resting-state formin on the cell surface as well as a decrease in actin polymerization (Ma et al., 2021), suggesting the occurrence of CW constraint-mediated formin clustering.

In contrast, plant PTI activation induces the local recruitment and immobilization of type-I formins and induces higher order oligomerization of formin proteins through intermolecular interactions of formin dimers. Such local condensation and stabilization directly activate formin to exert its function in actin nucleation, which was demonstrated through in vivo imaging and in vitro reconstitution to generate multivalent formin proteins via protein engineering (Ma et al., 2021). During such PTI signaling, AC integrity is involved in the clustering of surface formin where the disruption of the AC by latrunculin attenuates the effects of PAMPs on formin clustering (Ma et al., 2021).

AC-mediated formin clustering on the cell surface is consistent with the mammalian PM picket-fence model, in which the molecular dynamics of surface biomolecules are coupled to and regulated by the AC–PM continuum (Jaillais and Ott, 2020; Kalappurakkal et al., 2020; Kusumi et al., 2010). However, whether and how plant PM biophysical properties, such as fluidity and compartmentalization, are involved in regulating formin clustering during plant PTI signaling remains unknown. Nevertheless, such local condensation-induced activation of plant formin nucleators is reminiscent of neural wiskott-Aldrich syndrome protein (N-WASP) phase-separation that activates the branched actin nucleator actin-related protein (Arp) 2/3 complex and, thus, actin remodeling during immune responses in mammalian cells (Su et al., 2016; Case et al., 2019b). While such progressive assembly of the macromolecular complex to activate actin polymerization is well characterized in the

mammalian system, the underlying molecular mechanisms by which plant type-I formins are guided to form nanoclusters and remodel the AC remain enigmatic.

Macromolecular complex formation through biomolecular condensation has been recognized as an essential mechanism underlying protein functionalities in 3D space (Alberti et al., 2009; Xie et al., 2019; Emenecker et al., 2020; Xie et al., 2020; Xie and Miao, 2021) and on 2D cell surfaces, such as receptor activation and signal transduction (Su et al., 2016; Banani et al., 2017; Ojosnegros et al., 2017; Case et al., 2019a; Feng et al., 2019a; Wu et al., 2020; Zhao and Zhang, 2020). An increasing number of molecular factors have been proposed to influence the formation of distinct condensates from the surrounding milieu, including the complexity of constituents (Wang et al., 2018), biomolecular stoichiometry (Case et al., 2019b; Huang et al., 2019), posttranslational modifications (Miao et al., 2018), and spatiotemporal effects (Feng et al., 2019a, 2019b; Zeng et al., 2018).

The plant cell PM regulates its surface biophysical properties by forming nanometer-sized compartments and nanodomains, driven by lipid–lipid, lipid–protein, and multivalent protein–protein interactions (Raffaele et al., 2009; Huang et al., 2019; Jaillais and Ott, 2020; Ke et al., 2020; Tran et al., 2020). PM compartmentalization is characterized by the formation of spatially separated high-order lipid nanodomains that are enriched in saturated phospholipids, sterols, and sphingolipids, and a relatively packed and less dynamic lipid environment for residing membrane proteins (Sezgin et al., 2017). Various PM proteins, including receptor proteins and kinases, have been observed to form nanoclusters or to be regulated by nanodomains during signal transduction (Bücherl et al., 2017; Stone et al., 2017; Perraki et al., 2018; Abel et al., 2021).

In plants, one of the best-characterized bona fide nanodomain-residing proteins is remorin (Bariola et al., 2004; Raffaele et al., 2009; Jarsch et al., 2014). The PM association and macromolecular assembly of remorin have been characterized as critical properties involved in regulating nanodomain formation and remorin-involved biological processes, such as plasmodesmata gating in Arabidopsis (Perraki et al., 2018; Huang et al., 2019), surface clustering of receptors and auxin transporters (Bücherl et al., 2017; Gronnier et al., 2017; Ke et al., 2020), and stabilization of the LYK3 receptor in *Medicago truncatula* (Liang et al., 2018). The detailed molecular mechanisms by which remorin modulates self-assembly and macromolecular assembly with associated biomolecules have yet to be fully elucidated.

Here, we demonstrated that the macromolecular assembly of Arabidopsis remorin, indicating the degree of nanodomain formation, is increased progressively upon PTI activation, by showing increases in the clustering of AtREM1.2 and AtREM1.3. This increase in nanodomain assembly during PTI responses in a time-dependent manner drove formin clustering on the Arabidopsis PM and increased actin polymerization, both of which are remorin- and sterol-dependent. Furthermore, we found that the N-terminal

intrinsically disordered region (IDR) of remorin directly mediated its interaction with type-I formin, enabling formin recruitment and local condensation through the orchestrated multivalent interactions of remorin during PTI signaling activation. Via an artificial lipid bilayer-based reconstitution system, we recapitulated the macromolecular assembly of the remorin–formin complex and demonstrated remorin: formin stoichiometry-dependent activation of formin activities for actin nucleation. Altogether, our studies have revealed a mechanism by which the molecular assembly of remorin and remorin-resident nanodomains regulate formin recruitment and nanoclustering for actin remodeling during plant innate immune responses. Our work has revealed how macromolecular condensation mediated by lipid nanodomains acts as a signaling hub for multivalent biomolecular interactions that fine-tune signal transduction in a spatiotemporally regulated manner.

Results

Formin nanoclustering mediates actin remodeling during Arabidopsis PTI responses in a nanodomain-dependent manner

The upregulation of actin assembly by the flg22-triggered PTI response depends on the nanoclustering of type-I formins on the PM (Ma et al., 2021). To investigate how formin proteins are progressively and multivalently clustered during PTI activation, we studied the spatiotemporal regulation of formin dynamics on the Arabidopsis leaf epidermis cell surface in the presence of *Xanthomonas campestris* pv. campestris (*Xcc*), using a readily available stable transgenic Arabidopsis line expressing formin fused with a C-terminal GFP, *Pro35S:AtFH6-GFP* (termed AtFH6-GFP; Damme et al., 2004). Five-day-old (5 d) AtFH6-GFP-expressing seedlings were flood inoculated with 1×10^7 colony-forming units (CFU)/mL *Xcc* wild-type (WT) strain 8004 (*Xcc* 8004; Ishiga et al., 2011).

Before bacterial infection, AtFH6-GFP showed both diffuse and distinct punctate patterns, suggesting the occurrence of heterogeneous oligomers of the resting-state formin proteins (Supplemental Figure S1A). We quantitatively measured the total signal intensity of the punctate AtFH6-GFP particles, which reflects the degree of nanoclustering and the distribution of the oligomeric states of AtFH6 on the PM (Ma et al., 2021). After *Xcc* 8004 inoculation, we started to observe a gradual increase in the AtFH6-GFP intensity, starting at 0.5-h postinoculation (0.5 hpi) and reaching the highest nanoclustering peak at 3 hpi, during the early infection stage (Figure 1A; Supplemental Figure S1A).

We next treated 5–day-old Arabidopsis seedlings with 10-μM flg22. Interestingly, we observed similar temporal regulation of AtFH6-GFP nanoclustering to that recorded following *Xcc* 8004 inoculation (Figure 1A; Supplemental Figure S1B), suggesting that formin nanoclustering is progressively activated through PAMP-activated PTI signaling. As a negative control, AtFH6-GFP intensity in the seedlings
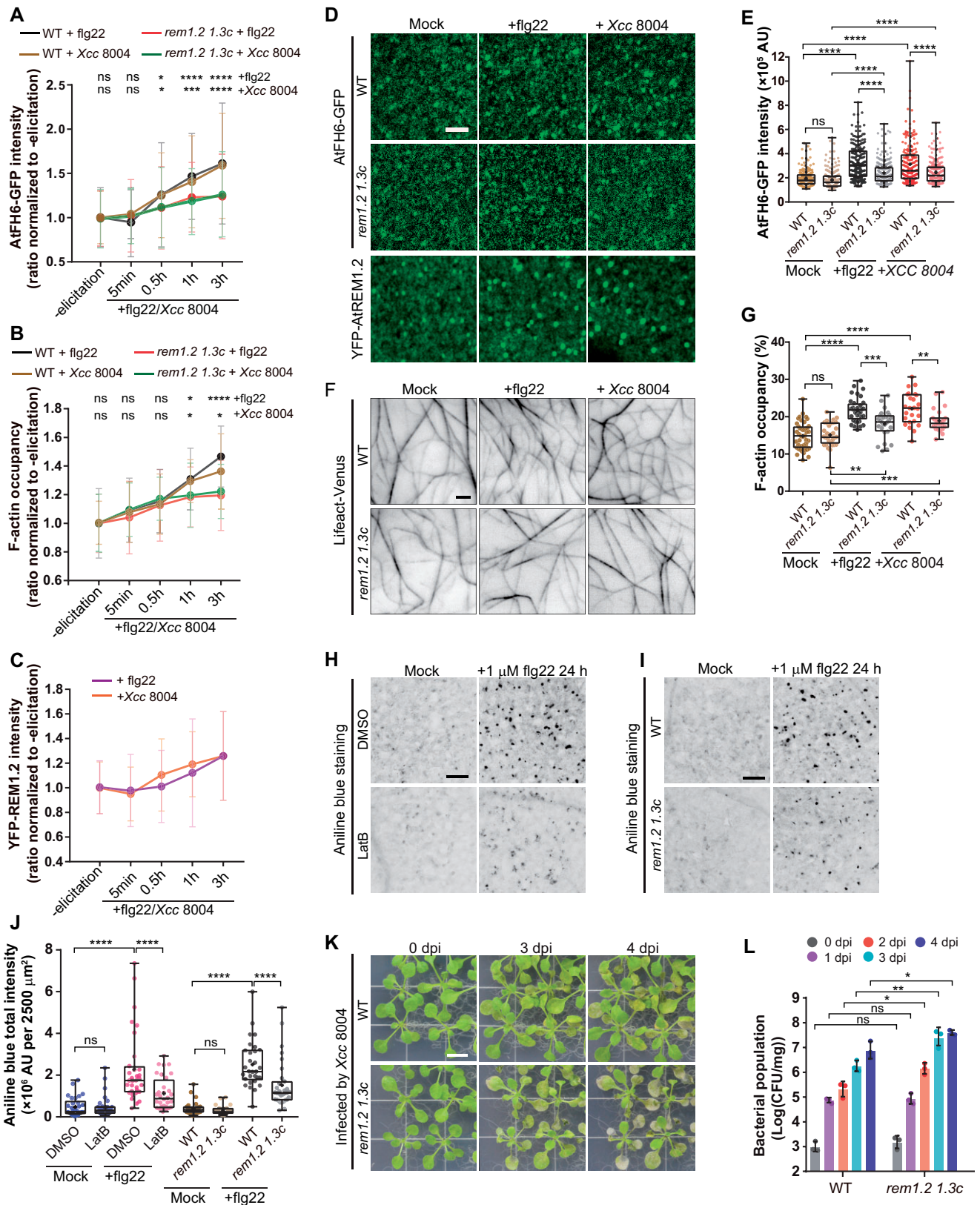
Figure 1 Remorin mediates formin clustering and actin polymerization for Arabidopsis PTI responses. A and B, Quantification of the total fluorescence intensity of AtFH6-GFP punctate foci (A) and Lifeact-Venus-labeled F-actin occupancy (B) on the cotyledon epidermal cell surface of 5-day WT and *rem1.2 1.3c* seedlings inoculated with 10-μM flg22 or 1 × 10⁷ CFU·mL⁻¹ *Xcc* 8004 at the indicated time point before and postinoculation. The particle intensities of AtFH6-GFP or F-actin occupancy were normalized to the mean values of the seedlings before *Xcc* 8004 or flg22 elicitation as ratios. Statistical analysis of AtFH6-GFP intensity or F-actin occupancy in the WT and *rem1.2 1.3c* seedlings at each time point is shown on top of the related chart. *n* = 200 particles in (A), *n* > 25 cells in (B). C, Quantification of the total fluorescence intensity of YFP-AtREM1.2 in 5-day

without *Xcc* 8004 inoculation or flg22-elicitation did not show apparent change (Supplemental Figure S1C). In addition, another well-studied PAMP, elf26, obviously triggered AtFH6-GFP nanoclustering, whereas flgII28, a flagellin-derived epitope that is not recognized by Arabidopsis (Hind et al., 2016), showed no effects on AtFH6-GFP nanoclustering (Supplemental Figure S1, D and E), further supporting the conclusion of AtFH6-GFP condensation by PTI activation.

We additionally tested whether PAMP-triggered AtFH6 condensation also applies to other type-I formins. We examined another stable transgenic line AtFH2-eGFP (Diao et al., 2018) under the control of the native promoter, which displays relatively more diffused patterns on the PM compared to 35S promoter-driven AtFH6. To quantitatively analyze the clustering effect of AtFH2-eGFP by immune-elicitation, we analyzed the spatial clustering index (SCI; Gronnier et al., 2017) of AtFH2-eGFP, which demonstrated clear nanoclustering of AtFH2-eGFP upon *Xcc* 8004 infection, flg22 elicitation and elf26 elicitation after 3h, while flgII28 treatment did not show any obvious clustering of AtFH2 (Supplemental Figure S1, F and G).

We next imaged the F-actin arrays in Arabidopsis seedlings expressing *Pro35S:Lifeact-Venus* (termed Lifeact-Venus; Era et al., 2009). Accordingly, a similar time-dependent increase in F-actin occupancy was observed in both *Xcc* 8004- and flg22-elicited (Figure 1B; Supplemental Figure S1, A and B) seedlings. However, neither *Xcc* 8004 nor flg22 increased F-actin bundling, as indicated by skewness analysis over the monitoring period (Supplemental Figure S1H), which is consistent with previous reports showing plant PTI-specific responses triggering F-actin density but not bundling increase (Henty-Ridilla et al., 2013, 2014; Sun et al., 2018b; Ma et al., 2021). As controls, inoculating the seedlings with the buffer for suspending bacteria did not induce obvious changes in F-actin organization within the same monitoring period of bacterial treatment (Supplemental Figure S1, I and J). Taken together, these results suggest dynamic complex assembly and a gradual increase in the nanocondensation of formins during host PTI responses in a spatiotemporally regulated manner.

Plant type-I formins are integrated into multiple layers of scaffolds in the CW–PM–AC continuum. A previous report demonstrated that CW biosynthesis modulates formin nanoclustering through physical associations (Ma et al., 2021). However, although PAMP flg22 induces formin clustering, it does not change cellulose production (Ma et al., 2021), suggesting additional unknown mechanisms regulating formin nanoclustering upon PTI activation. Given the emerging roles of plant nanodomains in regulating molecular condensation and protein functions in cell signaling events (Garcia-Parajo et al., 2014; Sezgin et al., 2017; Jaillais and Ott, 2020; Abel et al., 2021), we were motivated to ask whether the lipid nanodomain is involved in PTI-triggered formin nanoclustering.

First, we treated Arabidopsis seedlings with 10-mM methyl-β-cyclodextrin (MβCD), a commonly used sterol-depleting and nanodomain-disrupting agent (López et al., 2011). MβCD treatment resulted in a significant reduction in the signal intensity of YFP-AtREM1.2, a lipid nanodomain marker (Supplemental Figure S2, A and B; Jarsch et al., 2014; Huang et al., 2019), indicating impaired structural assembly and stability of nanodomain compartments. Interestingly, the same MβCD condition also decreased the nanoclustering and confined-lateral diffusion of AtFH6-GFP triggered by PAMP flg22, indicating nanodomain-dependent formin nanoclustering during PTI (Supplemental Figure S2, C–G).

A single-particle analysis of AtFH6-GFP imaged via variable angle-total internal reflection fluorescence microscopy (VA-TIRFM; Supplemental Figure S2E) showed that MβCD increased AtFH6-GFP lateral diffusion, resulting in a higher mean squared displacement (MSD) and diffusion coefficient, and blocked the flg22-induced stabilization of AtFH6-GFP (Supplemental Figure S2, E–G and Supplemental Movie S1). Accordingly, the flg22-triggered increase in F-actin occupancy was also significantly attenuated in MβCD-treated seedlings (Supplemental Figure S2, H and I). These results collectively demonstrated that formin nanoclustering and the consequent increase in actin polymerization during PTI responses were directly dependent on PM nanodomain assembly.

Figure 1 (Continued)
seedlings inoculated as in (A) (see also Supplemental Figure S1, A and B). Normalized data were plotted as in (A). $n = 200$ as in (A). D, Representative images of AtFH6-GFP in the WT or *rem1.2 1.3c* and YFP-AtREM1.2 at 3 hpi after flg22 or *Xcc* 8004 treatment. E, Total intensity quantification of the AtFH6-GFP particles in (D), $n = 200$ particles. F, VA-TIRFM recording of Lifeact-Venus in the cotyledon epidermal cells of 5-day WT and *rem1.2 1.3c* seedlings elicited with flg22 or *Xcc* 8004 at 3 hpi, (G) Quantification of F-actin occupancy in (F), $n > 25$ cells. H–J, Callose deposition (H and I) and quantification (J) at the cotyledon surface in 2-week-old WT and *rem1.2 1.3c* seedlings treated with different combinations of 250-nM LatB (H) and 1-μM flg22 for 24 h before aniline blue-staining and imaging. ROIs (50 μm × 50 μm) were used for total intensity quantification. $N > 30$ ROIs. K, Disease symptoms of 2-week-old WT or *rem1.2 1.3c* seedlings with flood-inoculation with 1×10^7 CFU·mL^{-1} *Xcc* 8004 for 1 min. Representative images at 0 days postinoculation (0 dpi), 3 dpi, and 4 dpi are shown. L, Quantification of the internal *Xcc* 8004 bacterial population in the seedlings of (K) at the indicated time points. $N = 3$ individual seedlings. Significant differences were determined via one-way analysis of variance (ANOVA) with multiple comparisons (****$P \leqslant 0.0001$, ***$P \leqslant 0.001$, **$P \leqslant 0.01$, *$P \leqslant 0.05$, ns = not significant). Error bars = SD in (A), (B), (C), and (L). Scale bar: 2 μm in (D) and (F), 100 μm in (H) and (I), 0.5 cm in (K).

PAMP-triggered formin nanoclustering is dependent on remorin

We next sought to identify the determinative factor in the nanodomain regulating PAMP-triggered formin nanoclustering and actin polymerization. It has become increasingly clear that lipid nanodomain-residing remorin family proteins act as key regulators to modulate diverse host immune pathways, including receptor stabilization (Liang et al., 2018), kinase activation (Perraki et al., 2018), and plasmodesmata closure (Huang et al., 2019). Intriguingly, we observed a PTI-dependent clustering of AtREM1.2 (Supplemental Figure S1, A and B and Supplemental Figure S3, A and B) and AtREM1.3 (Supplemental Figure S3, C and D), the two most abundant remorin homologs in Arabidopsis (Jarsch et al., 2014), following treatment with *Xcc* 8004 and flg22 under the same conditions applied when examining AtFH6-GFP. In a quantitative analysis of the total intensity of YFP-AtREM1.2 puncta on the cell surface, YFP-AtREM1.2 showed an almost identical time-dependent pattern of progressive nanoclustering to AtFH6-GFP (Figure 1, A and C; Supplemental Figure S1, A and B). Accordingly, both YFP-AtREM1.2 and YFP-AtREM1.3 could be clustered through elicitation using the elf26 but not flgII28 peptide (Supplemental Figure S3, A–D).

The similar macromolecular assembly of remorin and formin upon PTI signaling with similar temporal regulation motivated us to ask whether remorin could directly regulate formin nanoclustering. Hence, we crossed AtFH6-GFP with the *rem1.2 1.3c* double mutant line, in which AtREM1.2 and AtREM1.3 were knocked out by T-DNA insertion and Clustered Regularly Interspaced Short Palindromic Repeats (CRISPR)–Cas9-based genome editing, respectively (Huang et al., 2019). When AtFH6-GFP/*rem1.2 1.3c* was inoculated with *Xcc* 8004 or flg22, we found that the time-dependent condensation of AtFH6-GFP was attenuated compared with that in WT seedlings (Figure 1A; Supplemental Figure S1, A and B). At 3 hpi of *Xcc* 8004 inoculation or flg22 elicitation, AtFH6-GFP showed a significantly lower intensity in *rem1.2 1.3c* than in WT plants (Figure 1, D and E). When the Lifeact-Venus-expressing seedlings were inoculated with the same concentration of *Xcc* 8004 or flg22 at which AtFH6-GFP was applied, the gradual increase in F-actin occupancy in the WT was also reduced in *rem1.2 1.3c* (Figure 1B; Supplemental Figure S1, A and B), as shown by a significantly lower F-actin occupancy at 3 hpi (Figure 1, F and G). However, without PAMP flg22 elicitation or *Xcc* 8004 infection, the AtFH6-GFP particle intensity was comparable in the WT and *rem1.2 1.3c* (Figure 1, D and E), indicating a similar assembly of resting-state formins in the two genetic backgrounds without PTI activation. Accordingly, we did not observe a difference in Lifeact-Venus-labeled F-actin occupancy or actin bundling between *rem1.2 1.3* and WT (Figure 1, F and G; Supplemental Figure S1K). These data demonstrated that formin nanoclustering and the consequent increase in actin assembly mediated by host PTI responses are highly dependent on remorin.

The rapid increase in host actin polymerization has been characterized as a hallmark of plant PTI responses (Henty-Ridilla et al., 2013; Sun et al., 2018b). We next sought to investigate the functional importance of formin nanoclustering and actin assembly underpinning plant PTI responses. Hence, we carried out aniline blue staining to study actin-dependent callose deposition, a well-defined plant PTI response, upon PAMP flg22-stimulation (Luna et al., 2011; Tran et al., 2020). We found that the induction of callose deposition by 1-μM flg22 treatment for 24 h was dramatically decreased by coincubation with 250-nM LatB (Figure 1, H and J), which has been verified to effectively disrupt the AC (Ma et al., 2021), demonstrating the crucial role of the AC in mediating plant PTI responses. Accordingly, we observed an attenuation of flg22-triggered callose deposition in *rem1.2 1.3c* (Figure 1, I and J), in which flg22-triggered actin assembly was impaired (Figure 1, B, F, and G).

Next, we carried out a bacterial flood inoculation assay to evaluate Arabidopsis susceptibility to *Xcc* 8004 infection with or without F-actin perturbation. As a result, we detected increased bacterial populations in both Latrunculin B (LatB)-treated WT and nontreated *rem1.2 1.3c* seedlings (Figure 1, K and L; Supplemental Figure S3, E and F), indicating increased susceptibility to bacterial infection upon the disruption of actin integrity and remorin functions. Moreover, we examined the rate of bacterial growth on plants after *Xcc* 8004 inoculation in seedlings that were treated with the formin inhibitor SMIFH2, which inhibits interactions between formin dimers and thereby blocks flg22-triggered formin nanoclustering but does not entirely abolish actin polymerization (Ma et al., 2021). SMIFH2-treated plants also showed lower flg22-induced callose deposition and greater bacterial growth than nontreated seedlings (Supplemental Figure S3, E–H), further supporting the function of formin nanoclusters in plant defense during plant–microbe interactions.

Taken together, the above results consistently demonstrated an attenuated defense mechanism in Arabidopsis seedlings with impaired formin-nanoclustering, actin polymerization, or remorin protein functions, supporting the interconnection of these functions in host PTI responses.

Progressive assembly of formin into nanoclusters promotes actin nucleation in vivo

We next sought to investigate whether the macromolecular assembly of nanodomain remorin proteins could directly recruit formin and lead to progressive nanoclustering and increased formin activity in vivo. We first coexpressed AtREM1.2 native promotor driven mScarlet-tagged AtREM1.2 (*ProREM1.2:mScarlet-AtREM1.2*) and AtFH6-GFP in the *rem1.2* background. Similar to the YFP-AtREM1.2 signal (Supplemental Figure S1A), we observed a heterogeneous diffusion or punctate pattern of mScarlet-AtREM1.2 on the PM, which did not show an apparent association with AtFH6-GFP particles (Figure 2A).
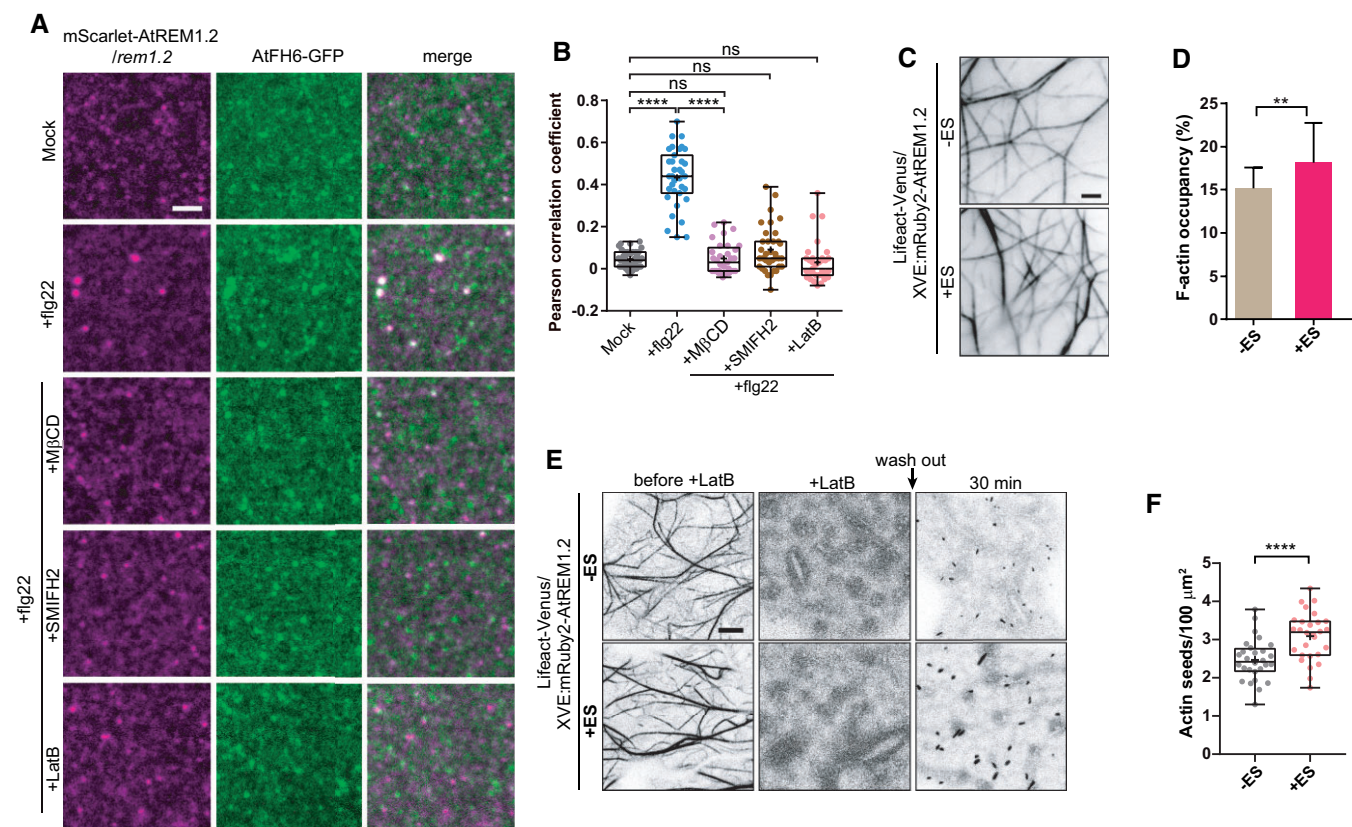
Figure 2 Remorin recruits formin for clustering and promotes formin actin nucleation activity. A, mScarlet-AtREM1.2 (magenta) and AtFH6-GFP foci (green) on the cotyledon epidermal cell surface in 5 d *AtFH6-GFP/ProREM1.2:mScarlet-AtREM1.2/rem1.2* seedlings, with or without 3 h of flg22 treatment with 10 μM (upper two parts). The lower three parts are the seedlings that were treated by 10-μM flg22 together with 10-mM MβCD, 50-μM SMIFH2, or 5-μM LatB for 3 h before imaging. B, Pearson correlation coefficient analysis of AtFH6-GFP and mScarlet-AtREM1.2 foci in the seedlings as in (A). $n > 30$ ROIs (20 μm × 20 μm in size). C, Representative VA-TIRFM images of Lifeact-Venus-labeled F-actin in cotyledon epidermal cells of 5 d *Lifeact-Venus/XVE:mRuby2-AtREM1.2* seedlings with or without 24 h ES treatment at 5 μM. D, Quantification of F-actin occupancy from (C). $n > 40$ cells. Error bars = SD. E, CLSM recording of F-actin regeneration in *Lifeact-Venus/XVE:mRuby2-AtREM1.2* seedlings. Five-day-old seedlings were inoculated, with or without 5-μM ES for 24 h, before an additional 40 min of LatB treatment at 5 μM to completely disrupt F-actin. Regenerated actin seeds were imaged 30 min after LatB washout. F, Quantification of actin seed numbers at 30 min after LatB washout from (E). $n = 30$ cells. Significant differences were determined via Student's t test assuming equal variances in (D) and (F), or one-way ANOVA with multiple comparisons in (B) (****$P \leqslant 0.0001$, ***$P \leqslant 0.0001$, **$P \leqslant 0.01$, ns = not significant). Scale bar: 2 μm in (A) and (C), 5 μm in (E).

Interestingly, we observed that 10-μM flg22 but not flgII28 elicitation for 3 h induced the clustering of both mScarlet-AtREM1.2 and AtFH6-GFP, which are highly colocalized by showing a Pearson's correlation coefficient $R = 0.43 \pm 0.14$ (Figure 2, A and B; Supplemental Figure S3, I and J). Such colocalization could be significantly abolished by either MβCD, SMIFH2, or LatB coinoculation (Figure 2, A and B), suggesting nanodomain assembly-, interactions between AtFH6 dimers-, and cortical AC integrity-dependent AtREM1.2–AtFH6 complex formation during PTI signaling. In contrast, coinoculation with DMSO or CK666, which inhibits another actin nucleator Arp2/3 complex (Hetrick et al., 2013), did not affect flg22-triggered AtREM1.2–AtFH6 complex association and clustering (Supplemental Figure S3, I and J). Consistently, the CK666 treatment did not change flg22-triggered actin remodeling (Supplemental Figure S3, K–M).

Next, to better mimic the gradual PTI-triggered assembly of remorin proteins into nanodomains, we developed

another Arabidopsis transgenic line that coexpresses mRuby2-AtREM1.2 under the control of a β-estradiol (ES)-inducible promotor (*XVE:mRuby2-AtREM1.2*) and AtFH6-GFP through *Agrobacterium*-mediated transformation. mRuby2-AtREM1.2 expression was induced in 5-day seedlings by treatment with 5-μM ES for 24 h. Under such conditions, apparent increases in protein expression and oligomerization were observed by imaging mRuby2-AtREM1.2 fluorescence on the PM (Supplemental Figure S4, A and B), consistent with the previously reported phenotype of XVE:AtREM1.2 (Huang et al., 2019).

In alignment with the above flg22-triggered mScarlet-AtREM1.2 and AtFH6-GFP complex clustering and colocalization, the induced punctate mRuby2-AtREM1.2 assemblies on the PM also largely colocalized with AtFH6-GFP nanoclusters on PM (Supplemental Figure S4, A and C). By measuring the signal intensity of formin punctate foci, we found that AtFH6-GFP nanoclustering was significantly increased in AtREM1.2 overexpressing seedlings (Supplemental Figure

S4D), and that the degree of the increase in AtFH6-GFP nanoclustering was positively correlated with the degree of mRuby2-AtREM1.2 condensation (Supplemental Figure S4E). Accordingly, a single-particle analysis of AtFH6-GFP foci under VA-TIRFM imaging revealed significantly lower motility in the AtREM1.2 overexpression line (Supplemental Figure S4, F–H and Supplemental Movie S2). AtREM1.2-overexpression-induced condensation of AtREM1.2–AtFH6 remained unchanged after LatB treatment (Supplemental Figure S4, A, C, and D), demonstrating actin network integrity-independent disassociation once AtREM1.2–AtFH6 complex condensates formed. Together, these data suggested the occurrence of nanodomain assembly- or remorin assembly-dependent recruitment and condensation of formins.

We next tested the consequences of actin polymerization by increasing remorin assembly, which induces formin nanoclustering. We generated a stable transgenic Arabidopsis line coexpressing inducible mRuby2-AtREM1.2 and stable Lifeact-Venus. Upon the induction of AtREM1.2 overexpression by 5-µM ES in 5-day seedlings, VA-TIRFM revealed an increase in actin polymerization in vivo by showing higher F-actin occupancy compared to that in ES-untreated samples (Figure 2, C and D), suggesting a potential increase in the biochemical activity of formin in actin polymerization. Interestingly, around 40% of mRuby2-AtREM1.2 condensates directly associate with F-actin (Supplemental Figure S4, I and J), suggesting physical association between F-actin and formin–remorin complex as mRuby2-AtREM1.2 forms complex association with AtFH6-GFP (Supplemental Figure S4A). Such formin-F-actin association has also been previously reported in yeast by showing that Bni1 foci could localize on the actin cables by attaching to the F-actin barbed end (Buttery et al., 2007).

To further dissect whether the increase in actin polymerization under AtREM1.2 overexpression is derived from the change in the specific actin nucleation activity of formin or possible other later actin polymerization steps, we conducted an actin repolymerization experiment following LatB treatment and washout, which allowed us to directly evaluate the re-initiation of F-actin assembly to assess actin nucleation activities (Sun et al., 2021). F-actin was first depolymerized by treatment with 5-µM LatB for 40 min in 5-day seedlings co-expressing Lifeact-Venus and ES-induced mRuby2-AtREM 1.2, which were then subjected to a follow-up LatB washout to allow a repolymerization of the AC (Figure 2E). At ∼30 min post-LatB washout, we observed regeneration of short actin filaments (actin seeds; Figure 2E). Induction of AtREM1.2 overexpression resulted in an increased number of actin seeds under the same condition, indicating higher actin nucleation activities than that were observed in the noninduced seedlings (Figure 2, E and F). Together, these data collectively suggested that the macromolecular assembly of remorin directly recruits and condenses formins into nanoclusters to increase actin nucleation in vivo.

AtREM1.2 directly interacts with and condenses type-I formins to promote actin nucleation in vitro

We next sought to investigate whether the aforementioned AtREM1.2 assembly-mediated formin condensation and activation observed in vivo involve a physical interaction between formin and remorin. Here, to mimic the membrane-associated states of remorin and formin in vivo, we developed a supported lipid bilayer (SLB)-based in vitro reconstitution system to study remorin–formin interactions on the lipid bilayer surface, as well as potential formin condensation and activation of nucleation activities via macromolecular assembly. Since the AtFH6-FH1COOH recombinant protein (293–899 aa, termed FH6C hereafter; Supplemental Figure S5A) is not biochemically active in vitro (Ma et al., 2021; although it is indeed active in vivo with a capability to complement the formin function (Favery et al., 2004)), we utilized the biochemically active type-I Arabidopsis formin AtFH1 as a representative formin for in vitro reconstitution assays (Ma et al., 2021; Michelot et al., 2006, 2005; Sun et al., 2018b). We expressed and purified recombinant full-length AtREM1.2 (REM hereafter) and AtFH1-FH1COOH (430–1,051 aa, FH1C hereafter; Ma et al., 2021; Figure 3A; Supplemental Figure S5A).

First, we identified a moderate binding affinity between the recombinant REM and FH1C proteins, with a K_D = 369 nM, using a fluorescence anisotropy assay (Figure 3B). Second, we reconstituted the interplay between REM and FH1C on SLBs to recapitulate their native membrane integration and association. In this SLB-based reconstitution system, REM was associated with SLB through the C-terminal cysteine by coupling with Maleimido-DOPE (MCC-PE), which mimics the C-terminal cysteine lipidation-based membrane anchoring of remorin (Gronnier et al., 2017), whereas FH1C was physically linked to 1,2-dioleoyl-sn-glycero-3-[(N-(5-amino-1-carboxypentyl) iminodiacetic acid) succinyl] (nickel salt, DGS-NTA-Ni) in the SLB through a histidine-based terminal tag (Supplemental Figure S5B). A fixed quantity of FH1C protein was fluorescently labeled, anchored to the SLB and titrated with increasing concentrations of the REM protein where the stoichiometric ratios ranged from 1:0.25 to 1:8 (Figure 3C; Supplemental Figure S5C), as formin has been shown to be condensed by overexpressed but not native promoter-produced AtREM1.2 at the resting-states in vivo (Figure 2A; Supplemental Figure S4A).

The REM-mediated clustering of formin proteins on the 2D surface was characterized via TIRFM imaging and quantitively analyzed by measuring the total intensity of FH1C nanoclusters. We found that the FH1C assemblies were progressively condensed into higher order nanoclusters on the SLB in a REM-formin stoichiometry-dependent manner (Figure 3, C and D; Supplemental Figure S5, C and D). REM is able to condense FH1C starting from 1:0.5 of FH1C:REM stoichiometric ratio, suggesting effective multivalent binding that facilitates inter- and intramolecular interactions for remorin–formin complex assembly with a REM:FH1C stoichiometric ratio lower than 1:1. By investigating the
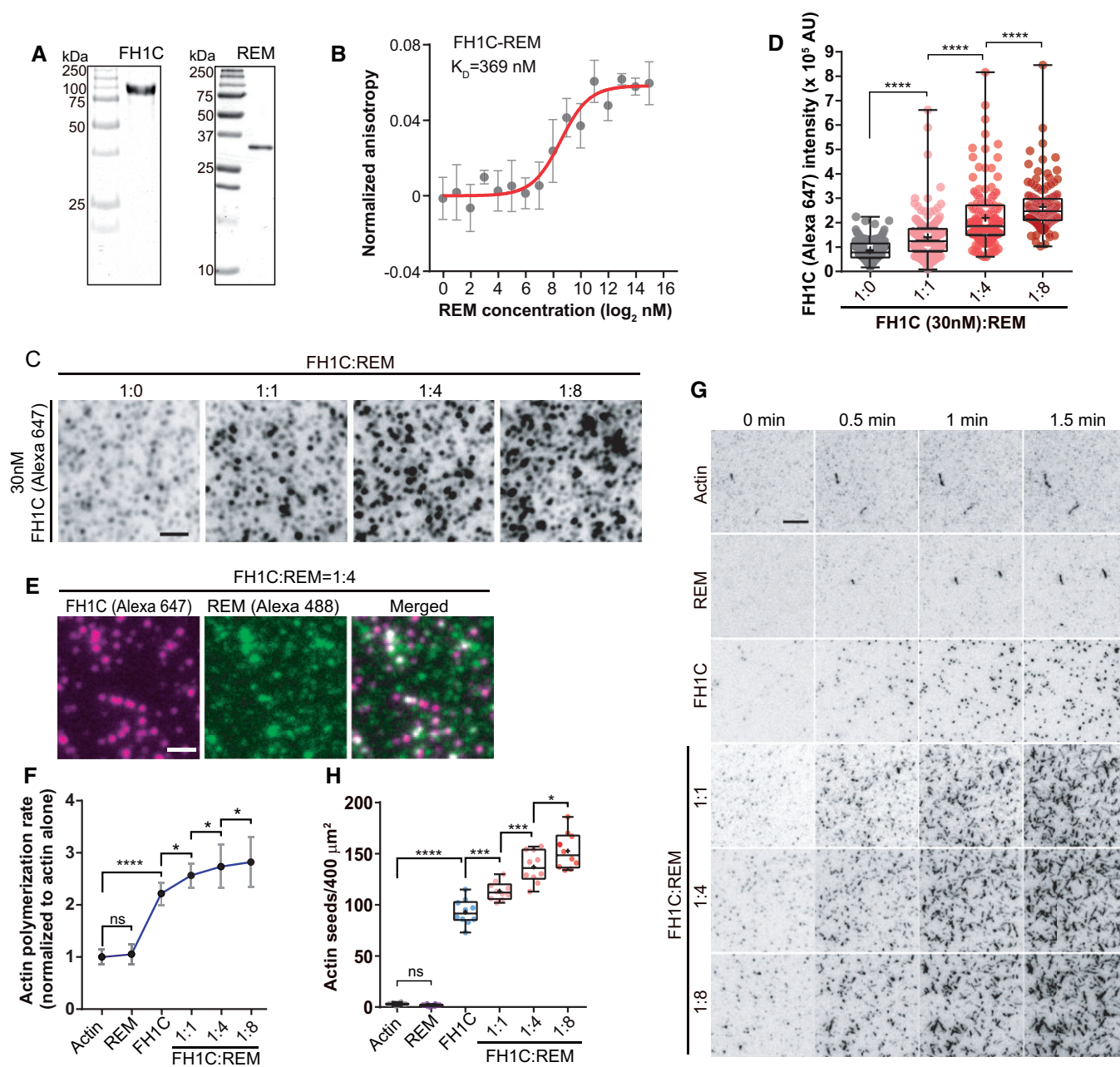
Figure 3 AtREM1.2 interacts with type-I formin and promotes formin-mediated actin nucleation in vitro. A, Coomassie blue-stained SDS–PAGE of recombinant AtFH1-FH1COOH (430–1,051 aa) (FH1C) and AtREM1.2 FL (REM) proteins. B, Fluorescence anisotropy assay of FH1C and REM interaction by mixing serial concentrations of REMs with a fixed concentration of 90-nM FH1C (labeled by Alexa Fluor 647 dye) for 20 min before measurement. The data were plotted with the Hill slope equation. $n = 3$ biological replicates. Error bars = SD. C, TIRFM recording of single-molecule images of FH1C mixed with titrated REM on SLBs. FH1C (30 nM, 10% Alexa 647-FH1C) was premixed with REM in protein buffer (20-mM HEPES, pH 7.4, 150-mM NaCl) at 1:0, 1:1, 1:4, and 1:8 stoichiometric ratios and further applied to SLBs for 2 min before imaging. D, Quantification of the single-particle total intensity of FH1C in (C). $n = 200$ particles. E, Representative TIRFM images of FH1C (10% Alexa 647-FH1C) and REM (10% Alexa 488-REM) on SLBs with a stoichiometric ratio of 1:4, as in (C). F, Relative actin polymerization rate in the pyrene-actin polymerization assay in the presence of 400-nM REM, 50-nM FH1C, or 50-nM FH1 plus REM at stoichiometric ratios 1:1, 1:4, and 1:8 (see also Supplemental Figure S5I). The data were normalized according to the spontaneous actin polymerization rate. $N = 6$ biological replicates. Error bars = SD. G, Representative images from the TIRFM actin polymerization assay in the presence of 240-nM REM alone or 30-nM FH1C with serial concentrations of REM at 1:1, 1:4, and 1:8 stoichiometric molar ratios, and 0.5-μM actin (10% Oregon green 488-actin and 0.5% biotin–actin). H, Quantification of the actin seed number at the 1 min time point in (G). $n = 10$ ROIs (20 μm $\times$ 20 μm in size). Significant differences were determined using one-way ANOVA with multiple comparisons in (D) and (H), or Student's t test assuming equal variances in (F) (****$P \leqslant 0.0001$, ***$P \leqslant 0.001$, *$P \leqslant 0.05$, ns = not significant). Scale bar: 5 μm in (C) and (E), 2 μm in (G).

colocalization of FH1C and REM at a 1:4 stoichiometry, we found that the large formin nanoclusters were highly colocalized with REM assemblies on the SLBs (Figure 3E), reminiscent of the in vivo colocalization of formin and remorin upon remorin clustering by flg22 elicitation or overexpression (Figure 2A; Supplemental Figure S4A). A similar REM dose-dependent formin clustering on the SLB is also observed for FH6C, which directly interacts with REM at a K_D = 469.3 nM (Supplemental Figure S5, E–H), suggesting general roles of remorin in condensing different formin homologs on a lipid bilayer surface involving physical interactions.

Next, we examined remorin-mediated formin biochemical activities in actin assembly mediated by formin condensation. First, we characterized formin-mediated actin polymerization using the bulk pyrene–actin assay. While REM did not influence spontaneous actin polymerization on its own, REM supplementation along with 50-nM FH1C clearly promoted FH1C-mediated actin polymerization in a REM:FH1C stoichiometry-dependent manner (Figure 3F; Supplemental Figure S5I). Second, to differentiate nucleation and elongation in the bulk actin assembly assay, we monitored F-actin assembly in real-time under TIRFM. A significant increase in FH1C-mediated actin nucleation was observed by generating a greater number of actin filament seeds, when increasing amounts of REM protein were added (Figure 3, G and H). In contrast, REM alone did not influence actin seed production (Figure 3, G and H), confirming that REM promoted actin nucleation through condensing formin both in vivo and in vitro.

The IDR orchestrates high-order assembly of remorin and thus is important for formin clustering and actin nucleation

Remorin proteins have been well-established to present the characteristics of an N-terminal IDR, a central coiled-coil (CC) domain, and a C-terminal membrane anchoring region (REM-CA; Gronnier et al., 2017; Jaillais and Ott, 2020; Gouguet et al., 2021). Each region of remorin proteins has been extensively characterized regarding their physical–chemical properties, such as mediating protein homo or heterooligomerization and membrane association (Marín et al., 2012; Gronnier et al., 2017; Martinez et al., 2019). However, we know little about how each of those regions, especially the N-terminal long IDR, accounting for >50% of the total residues in AtREM1.2 (Supplemental Figure S6A), contributes to remorin-mediated protein complex condensation.

Due to the prevalent roles of IDR in molecular condensation (Miao et al., 2018; Case et al., 2019a; Xie et al., 2019, 2020; Wu et al., 2020), we were motivated to investigate whether and how IDR mediates the macromolecular assembly of remorin and remorin–formin complex condensation. First, we expressed and purified several recombinant REM-truncating variants, including IDR (1–121 aa), CC (122–161 aa), ΔIDR, and ΔCC (Figure 4, A and B). Through fluorescence anisotropy assays, we characterized their physical

interactions with the FH1C formin. REM-ΔCC showed a moderate affinity toward FH1C (K_D = 512 nM), which was similar to but slightly lower than that of full-length REM (REM-FL; K_D = 369 nM; Figures 4C and 3B). REM-ΔIDR showed a much-reduced affinity toward FH1C with K_D = 1,077 nM (Figure 4C). Interestingly, REM-IDR alone presented a direct interaction with FH1C with K_D = 981.3 nM (Figure 4C). In contrast, REM-CC alone did not show an obvious interaction with FH1C (Figure 4C). Together, both the N- and C-terminal halves of REM could weakly associate with FH1C independently, with a lower K_D than that of REM-FL in both cases (Figure 3B). This suggests that in addition to the interaction of the IDR with FH1C, the C-terminal half of remorin might also bind FH1C, suggesting potential inter- and intramolecular interactions within the REM–FH1C complex that could partially explain the higher affinity for REM-FL comparing with REM-IDR alone.

In addition, multivalency can increase specificity and affinity for biomolecular interactions (Kastritis and Bonvin, 2013; Errington et al., 2019). The high valency of remorin proteins might also increase the number of inter- and intramolecular interaction sites (Abel et al., 2021) and thereby offer multivalent cooperativity that contributes to the higher K_D of formin binding for REM-FL relative to REM-IDR. To test this hypothesis, we next examined whether the IDR mediates the macromolecular assembly of REM. Through a size-exclusion chromatography (SEC) analysis of the REM-truncating variant, we observed dramatic shifts in the elution peak for both REM-ΔIDR and REM-ΔCC relative to REM-FL (Figure 4D), indicating a significant decrease in protein oligomerization level without IDR or CC, which is consistent with previous biochemical or structural studies of remorin IDR and CC (Marín et al., 2012; Martinez et al., 2019). Our results reveal the critical role of REM-IDR in mediating high-order remorin oligomerization, which further modulates the macromolecular assembly of the formin–remorin complex. We also examined FH1C recruitment and condensation by REM proteins without the IDR or CC using an in vitro SLB-based reconstitution system (Supplemental Figure S6, B and C). In contrast to REM-FL (Figure 3, C–E), neither REM-DIDR nor REM-DCC was sufficient to condense FH1C on the lipid bilayer (Supplemental Figure S6, B and C).

Next, we sought to examine the influence of IDR deletion on AtREM1.2 assembly, formin nanoclustering, and actin polymerization in vivo. We generated several stable Arabidopsis lines expressing inducible mRuby2-AtREM1.2 ΔIDR, ΔCC, and ΔC-ter (C-terminal; 1–193 aa; Figure 4A). Notably, ΔCC and ΔC-ter were included as controls, and ΔC-ter lacks a fragment 194–212 aa, which is slightly shorter than the previously defined REM-CA (185–212 aa of AtREM1.2; Perraki et al., 2012; Gronnier et al., 2017). ΔCC and ΔC-ter are predicted to show impairment in remorin assembly and function based on their known functions in oligomerization and membrane association, respectively (Gronnier et al., 2017; Legrand et al., 2019; Martinez et al., 2019). The above remorin expression cassettes are integrated
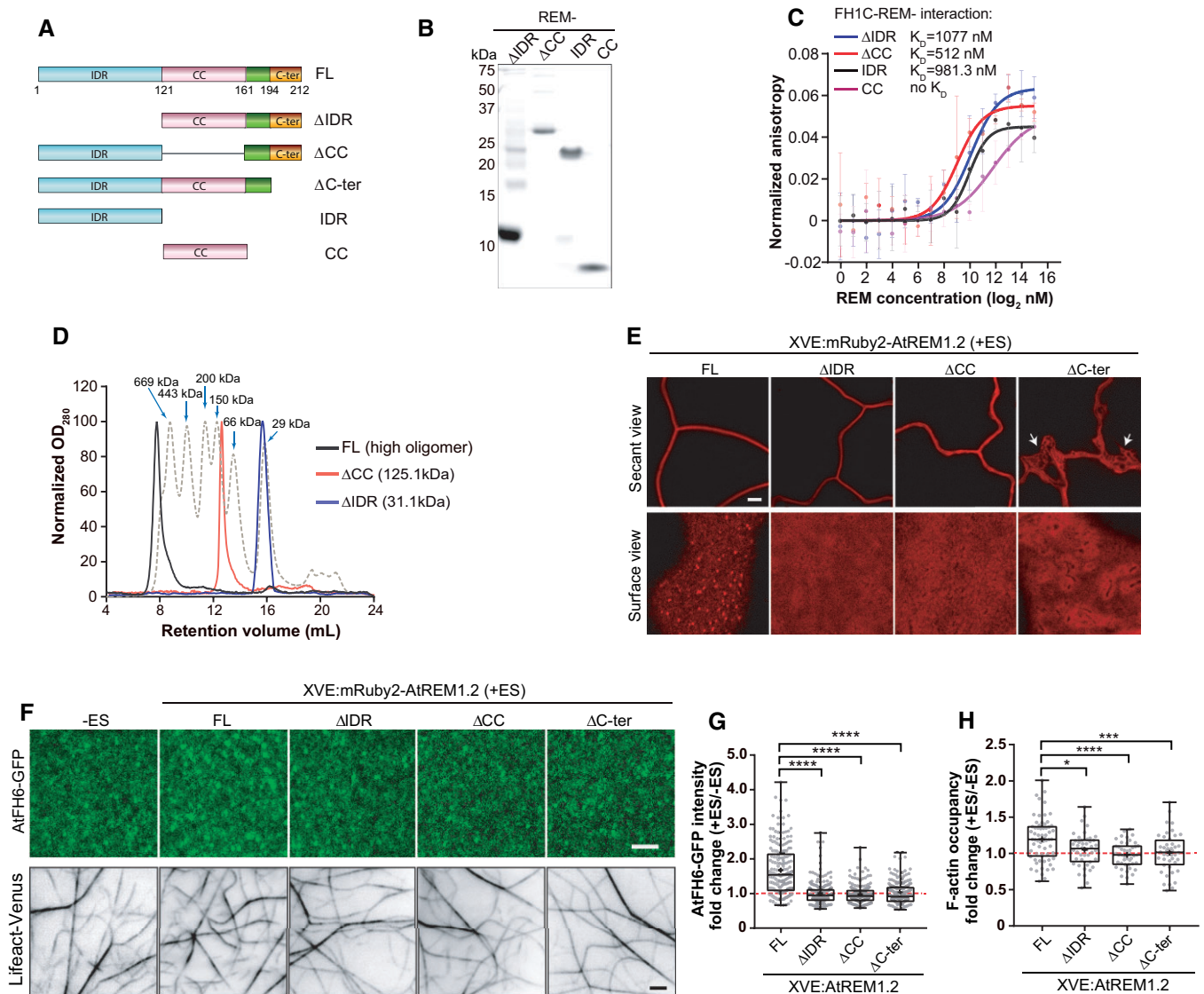
Figure 4 AtREM1.2 mediated type I formin clustering is dependent on high-order AtREM1.2 self-assembly. A, Domain schematics of AtREM1.2 (REM) FL and truncation variants. Predicted IDR, CC and C-ter were shown in different colors. B, Coomassie blue-stained SDS–PAGE of purified recombinant REM-ΔIDR and ΔCC truncated constructs and IDR and CC domains. C, Fluorescence anisotropy measurement of a fixed concentration of 90-nM FH1C (Alexa Fluor 647-labeled) mixed with serial concentrations of REM-truncating variants in protein buffer (20-mM HEPES, pH 7.4, 150-mM NaCl). The fluorescence anisotropy readouts of FH1C (Alexa 647) were plotted with the Hill slope equation. N = 3 biological replicates. Error bars = SD. D, Size exclusion chromatography profiles of recombinant REM-FL, ΔIDR and ΔCC proteins using a Superdex 200 10/300 GL column with calibration. The gray dashed line indicates the elution peaks of protein standards with the indicated sizes. The estimated size of each protein variant is shown in brackets, assuming a globular shape. E, Comparison of mRuby2-AtREM1.2 FL, ΔIDR, ΔCC, and ΔC-ter signals in vivo. Images were captured by CLSM in the cotyledon epidermal cells of 5 d XVE:mRuby2-AtREM1.2 FL, ΔIDR, ΔCC, and ΔC-ter transgenic seedlings, treated with 5-μM ES for 24 h before imaging. The secant view indicates the plasma membrane localization of mRuby2-AtREM1.2 FL, ΔIDR, and ΔCC, while the surface view reveals that only AtREM1.2 FL forms punctate foci. White arrows indicate cytosolic mRuby2 signal. F, Representative images of AtFH6-GFP foci and Lifeact-Venus-labeled F-actin in the seedlings with or without overexpression of the indicated AtREM1.2 truncating variants. Cotyledon epidermal cells of 5 day AtFH6-GFP/XVE:mRuby2-AtREM1.2 and Lifeact-Venus/XVE:mRuby2-AtREM1.2 seedlings overexpressing different REM variants (FL, ΔIDR, ΔCC, and ΔC-ter) subjected to 5-μM ES treatment for 24 h were imaged by CLSM or VA-TIRFM. G and H, Quantification of the fold changes in AtFH6-GFP particle total intensity (G) and F-actin occupancy (H) triggered by the overexpression of AtREM1.2 as in (F). n = 200 particles in (G) and n >40 cells in (H). Significant differences were determined using one-way ANOVA with multiple comparisons (****$P \leqslant 0.0001$, ***$P \leqslant 0.001$, *$P \leqslant 0.05$). Scale bar: 5 μm in (E), 2 μm in (F).

into AtFH6-GFP and Lifeact-Venus genetic backgrounds. Interestingly, unlike AtREM1.2 FL, which formed punctate clusters on the PM of cotyledon epidermal cells, AtREM1.2

ΔIDR showed a highly diffused signal on the PM without a punctate nanodomain pattern (Figure 4E), which was consistent with its low oligomerization status in vitro

(Figure 4D). Additionally, in accord with the in vitro results, we did not observe increased AtFH6-GFP nanoclustering or actin assembly after the overexpression of AtREM1.2 ΔIDR (Figure 4, F–H), whereas these changes were detected after the overexpression of AtREM1.2 FL (Figure 4, F–H). AtREM1.2 ΔCC showed similar effects to AtREM1.2 ΔIDR on self-assembly, formin clustering, and actin polymerization (Figure 4, D–H). In addition, AtREM1.2 ΔC-ter could not localize on the PM due to the lack of a C-terminal membrane anchoring (Figure 4E) and therefore did not induce increased AtFH6-GFP condensation or actin assembly, as expected (Figure 4, F–H). Taken together, our in vitro and in vivo data collectively suggested that the IDR-mediated high-order assembly of AtREM1.2 on the PM is one of the critical factors that orchestrates formin recruitment and nanoclustering for actin remodeling.

Discussion

During plant–microbe interactions, host immune responses trigger actin remodeling in two steps: the rapid increase in actin polymerization in early infection resulting from PAMP-mediated PTI signaling and the bundling of cortical F-actin by bacterial type III effectors in late infection stages (Henty-Ridilla et al., 2013). Actin remodeling and reorganization support numerous host processes contributing to defense mechanisms and have therefore been considered hallmarks of host PTI and effector-triggered immunity signal transduction (Li and Staiger, 2018). However, due to the complexity of signal transduction circuits, it remained unclear how bacterial-triggered host immune responses rapidly trigger actin remodeling until the recent identification of the underlying mediator: the PM-localized actin nucleation factor formin.

Recently, Arabidopsis type-I formin proteins have been found to be the underlying switches that activate actin assembly during PTI signaling by forming nanoclusters upon PAMP elicitation (Ma et al., 2021). Here, we have revealed the molecular mechanisms by which formins are converted into macromolecular condensates to activate actin polymerization during PTI signaling in a spatiotemporal-dependent manner (Figure 5). During plant immune signaling, such dynamic actin remoldling has been demonstrated to be involved in several fundamental cellular processes, including PM-associated immune precipitation, intra- or intercellular trafficking and transcriptional regulation of immune signaling, to coordinate multiple host defense mechanisms (Li and Day, 2019). In the meantime, the host AC is also a strategic point to be targeted by pathogen-derived molecules to perturb host actin assembly for pathogen invasion (Sun et al., 2021).

Coordinated regulation of molecular dynamics and condensation of type-I formins by the complex plant CW–PM–AC continuum

Because they are embedded within the multilayer CW–PM–AC continuum, type-I formins possess unique properties that allow them to sense a diverse array of changes in tensegrity, mechanical cues, and the biophysical properties of surface scaffolding structures. Such formin-sensing abilities provide broad surveillance functions in plants for various bacterial virulence factors that influence the plant CW–PM–AC continuum. For example, Xanthomonas diffusible signal factor increases Arabidopsis cellulose production, thereby perturbing CW constraints on formin motility and protein–protein interactions between formin dimers, resulting in an attenuation of actin polymerization (Ma et al., 2021). In contrast, PAMP flg22 stimulates formin nanoclustering without changing cellulose production in a manner that partially depends on the AC (Ma et al., 2021). We found that AC integrity is essential to support the macromolecular assembly of the formin–remorin complex, but plays a minimal role in complex disassociation. The well-structured filaments and networks of the AC might act as the supporting scaffold to guide the molecular dynamics for condensation and
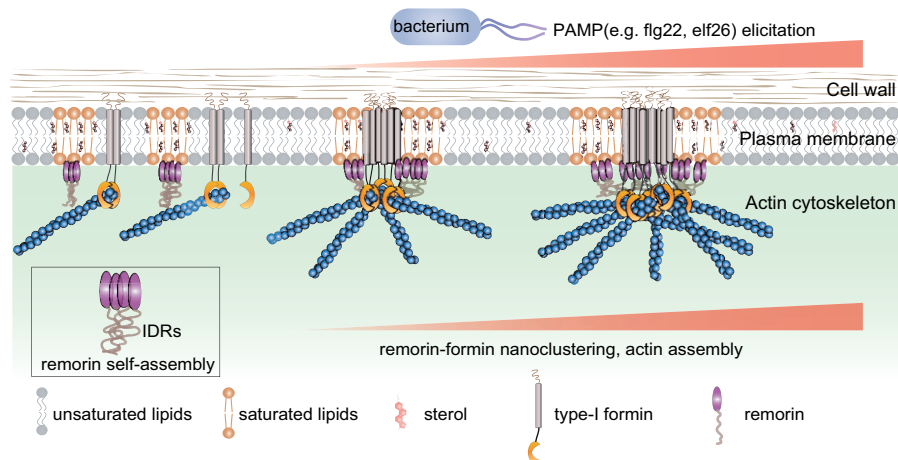
Figure 5 Proposed working model of remorin-mediated formin nanoclustering and actin assembly. Type I formins are integrated within the CW–PM–AC continuum. Perception of PAMPs triggers local high-order assembly of remorins through IDR-mediated self-oligomerization and, thus, the recruitment and gradual condensation of formins, and resultant actin polymerization in a time-dependent manner.

thereafter maintain the local condensation of formin proteins, similar to the picket-fence actin meshwork model proposed in the mammalian system (Gowrishankar et al., 2012; Saha et al., 2015; Sil et al., 2020). However, such geometrically organized treadmilling of the AC per se is not necessary to drive formin nanoclustering. Formin condensation on the PM likely results from actin macromolecular interactions, in which the confinement force of macromolecular condensation is well coordinated with the mechanical properties of the AC, which is a mechanism that has also been recently proposed to explain formin condensation at the polarized cell tip in yeast (Xie and Miao, 2021).

PM compartmentalization regulates actin remodeling during plant innate immune responses

Here, we have solved lingering puzzles by elucidating the underlying mechanism by which formin nanoclusters are actively condensed through nanodomain assembly and remorin oligomerization. During PTI responses, the assembly of PM lipid nanodomains is gradually increased in a time-dependent manner postinfection, which tunes the physical–chemical properties of the PM, biomolecular dynamics on the cell surface, the active recruitment of formin into nanoclusters and, thus, the nucleation of the AC. PTI activation promotes macromolecular assembly within nanodomain structures. Such PTI-enhanced PM compartmentalization recruits and condenses partitioning cell surface biomolecules via larger confined nanodomains. As an abundant nanodomain-resident scaffolding protein, AtREM1.2 senses different signals and is able to form high-order oligomers that regulate the biophysical properties of PM, such as lipid compartmentalization (Huang et al., 2019). By studying Arabidopsis AtREM1.2, we identified molecular mechanisms of IDR-mediated remorin assembly and formin recruitment. AtREM1.2 IDR interacted with the cytosolic domains of formin and regulated formin clustering through remorin oligomerization and remorin–formin complex macromolecular assembly (Figure 5). The fluorescence anisotropy assay showed that the interaction between AtREM1.2 and formins was moderate in vitro. The inter- and intramolecular interactions are likely to be dramatically increased toward macromolecular assembly via cooperative binding (Kastritis and Bonvin, 2013; Errington et al., 2019).

Compared to solution assembly, PM association, which is another regulatory factor for biomolecular complex assembly, provides spatial regulation with surface stabilization and thereby facilitates macromolecular assembly on a 2D surface (Case et al., 2019a; Feng et al., 2019a; Xiao et al., 2021). The self-multivalency of remorin plays essential roles in driving formin clustering and increasing actin nucleation (Figure 4). IDRs guide the high-order self-oligomerization of remorin and the dynamic ensemble of remorin–formin complexes, which undergo intra- or intermolecular interactions and exhibit high-order assembly, via the interactive motifs within and outside of IDRs (Miao et al., 2018; Choi and Pappu, 2020). Our artificial lipid-bilayer-based in vitro assay

successfully recapitulated remorin–formin interactions on a 2D lipid surface in a protein dosage- and stoichiometry-dependent manner. Our successful reconstitution of the macromolecular assembly of the remorin–formin complex by 2D lipid surface anchoring suggests that the gradual recruitment and clustering of formin in remorin-residing nanodomains in vivo could result from the synergistic action of PM targeting through the transmembrane domain of formin (Diaz-Rohrer et al., 2014) and the high-order assembly of remorin proteins in an IDR-dependent manner.

IDRs serve as signaling hubs that regulate a diverse array of signal transduction pathways (Haynes et al., 2006; Wright and Dyson, 2015). IDRs can also undergo dynamic posttranslational modification, thus regulating protein oligomerization and protein activities (Miao et al., 2018). The N-terminal IDR regions of plant remorin also contain multiple phosphorylation sites that are crucial for remorin functionality during plant immune signaling (Marin and Ott, 2012; Gouguet et al., 2021). Recently, several other plant surface signaling molecules, such as the plant surface immune receptor FLAGELLIN SENSITIVE2 (Keinath et al., 2010; Bücherl et al., 2017) and the auxin transporter PIN-FORMED2 (Ke et al., 2020), have been shown to cross-talk with remorin-residing nanodomains, in which a perturbation of remorin interfered with the corresponding signaling transductions, although whether remorin directly interacts or regulates those surface molecules remains elusive. Previously, the remorin N-terminal IDR has also been reported to facilitate inter- and intramolecular interactions (Marin et al., 2012). Future studies need to identify the underlying mechanisms by which plant innate immunity could trigger remorin self-oligomerization and macromolecular assembly with formin or other associated proteins, and how posttranslational modification involved in complex assembly during signal transduction. These studies would require a systematic approach to understand how remorin IDRs engage in crosstalk with other nanodomain residents and drive molecular condensations on the cell surface in a time-dependent manner upon immune activation.

The plant immune response triggers biomolecular condensation on the cell surface, and the consequent induction of signal transduction and actin remodeling is reminiscent of what occurs in mammalian T-cell immune activation. The activation of T-cell receptor (TCR)-mediated cell signaling triggers the molecular condensation of several TCR-related signaling constituents, including PM-localized receptors, adaptors, scaffolders, and actin regulatory proteins (Su et al., 2016; Case et al., 2019b). Phase separation-mediated actin nucleator Arp2/3 complex condensation activates actin nucleation during T-cell signal transduction (Su et al., 2016; Case et al., 2019b). Such molecular condensation-regulated cytoskeleton remodeling has also been identified in other mammalian systems, such as the local enrichment of tubulin and resultant promotion of microtubule nucleation by the pericentriolar material scaffold protein SPD-5 and microtubule effector protein targeting protein for Xklp2 (TPX2),

respectively (Woodruff et al., 2017; King and Petry, 2020). Similarly, the oligomerization of VASP proteins enables the closer positioning of these proteins and, thus, their bound G-actins, which together facilitate actin filament elongation (Brühmann et al., 2017). It is unclear whether formin-type nucleators exhibit a similar mechanism in mammalian cells to the mechanism we have identified in the plant system. The integration of plant type-I formin within the CW–PM–AC continuum offers unique mechanisms of mechanical regulation that individually or cooperatively fine-tune the molecular dynamics and molecular condensation of actin nucleator formins under a diverse array of environmental and chemical cues in the 2D plane. In addition, plant-specific remorin proteins form spatially distinguishable nanodomain structures with tight confinement, which drive non-equilibrium conditions leading to molecular condensation and signal activation during plant immune responses.

Materials and methods

Plant growth
All the *Arabidopsis thaliana* seedlings used in this study were of the Columbia ecotype background. The seeds were first surface-sterilized in 15% bleach (v/v) for 1 min. After washing with autoclaved distilled water three times, the seeds were plotted on half-strength Murashige and Skoog (1/2 MS) medium supplied with 0.8% agar, pH 5.8, followed by stratifying at 4°C in the dark for more than 2 days before further growing in growth chambers (Percival, Model AR-95L2) under long-day conditions (8-h dark:16-h light with cool white light intensity as 150 μmol·m^{-2}·s^{-1}) at 22°C. 4- or 5-day-old seedlings were used for treatments and imaging, and 2- or 4-week-old seedlings were used for callose staining and bacterial flooding inoculation assays, genetic transformation, or crossing.

Generation of Arabidopsis transgenic lines
Arabidopsis stable transgenic lines: *AtFH6* (AT5G67470)-*GFP* and *Lifeact-Venus* are driven by the 35S promoter, whereas *YFP-AtREM1.2* (AT3G61260), *YFP-AtREM1.3* (AT2G45820), and *AtFH2* (AT2G43800)-*eGFP* are driven by their native promotors; these constructs and the *rem1.2 1.3c* mutants were generated in previous publications (Damme et al., 2004; Era et al., 2009; Jarsch et al., 2014; Diao et al., 2018; Huang et al., 2019). Plants carrying *AtFH6-GFP* (resistant to kanamycin) and *Lifeact-Venus* (resistant to hygromycin) were crossed with *rem1.2 1.3c* or *rem1.2*. Homozygous plants were screened by the related antibiotics, genotyping for *rem1.2* (Salk_117639), and sequencing verification for *rem1.3c* (Supplemental Table S1) generated by CRISPR–Cas9-mediated genome editing (Huang et al., 2019).

To construct an inducible promotor system, *XVE:mRuby2-AtREM1.2*, the *3xMyc-mRuby2-AtREM1.2* fragment, synthesized by Synbio Technologies (USA), was integrated into the PER10 backbone through Asc1 and Spe1 restriction enzyme digestion sites. *XVE:mRuby2-AtREM1.2* truncation variants ΔIDR, ΔC-ter, and ΔCC were generated by truncating the

AtREM1.2 N-terminal 1–363 bp, 583–636 bp, 364–483 bp fragments in FL version, respectively, through one-step PCR and ligation (primers listed Supplemental Table S1). These *XVE:mRuby2-AtREM1.2* variants were additionally transformed into AtFH6-GFP and Lifeact-Venus stable Arabidopsis lines through *Agrobacterium tumefaciens* GV3101-mediated transformation and floral-dip method. T3 homozygote lines screened by glufosinate ammonia were used for further experiments. To construct *ProREM1.2:mScarlet-AtREM1.2*, a mScarlet fragment with Arabidopsis codon optimization was synthesized by Synbio Technologies (USA) and was further integrated into a previous published *ProREM1.2:eGFP-AtREM1.2* vector (Huang et al., 2019) to substitute the eGFP fragment through XhoI and AscI restriction enzyme digestion sites. The sequencing verified vector was transformed to the AtFH6-GFP/*rem1.2* line as above. T3 Homozygotes were screened by glufosinate ammonia.

Chemical treatment
MβCD (methyl-β-cyclodextrin), LatB, SMIFH2, CK666, and ES were purchased from Sigma-Aldrich and dissolved in water, DMSO, or ethanol. The PAMP peptides flg22, elf26, and flgII28 (>98% purity) were synthesized by GL Biochem (China) and dissolved in water. Chemical treatments for 5 d Arabidopsis seedlings were carried out in 24-well plates by adding indicated concentrations of chemicals to liquid 1/2 MS medium. Then the seedlings were soaked in the medium at the indicated time before imaging. Treatments with the same volume of related solvent were used as controls. For bacterial flood-inoculation assay, 2-week-old seedlings in 1/2 MS plates were first soaked in distilled water supplied with DMSO, 250-nM LatB, and 50-μM SMIFH2 for 5 min, after which the distilled water was dumped off, and the plates were sealed and kept in the growth chamber for another 24 h treatments.

Bacterial inoculation
The *Xcc* was used in this study for bacterial inoculation and flood-inoculation assays (Ishiga et al., 2011). To image the temporal change in AtFH6-GFP and YFP-AtREM1.2, and YFP-AtREM1.3 during bacterial infection, a single clone of the *Xcc* WT 8004 strain (*Xcc* 8004) was cultured in NYG (3 g·L^{-1} yeast extract, 5 g·L^{-1} peptone, 20 g·L^{-1} glycerol) medium at 28°C overnight, followed by resuspension in 10-mM MgCl$_2$ supplied with 0.02% Silwet L-77 at a final concentration of 1×10^7 CFU·mL^{-1}. Five-day-old seedlings were then immersed into the bacterial suspension or only resuspension buffer for 1 min followed by inoculation under normal growth conditions described above before imaging at the indicated time points. For the flood-inoculation assay, 2-week-old seedlings of the WT, *rem1.21.3c*, or WT treated with DMSO, LatB, and SMIFH2 in 1/2 MS plates were flood inoculated with the same concentration of *Xcc* 8004 suspension or only resuspension buffer as described above for 1 min, after which Arabidopsis seedling disease symptoms were captured over the next 4 days.

In vivo image acquisition

To image AtFH6-GFP, AtFH2-eGFP, YFP-AtREM1.2/AtREM1.3 clustering during bacterial or PAMP inoculation and the colocalization of mScarlet- or mRuby2-AtREM1.2 and AtFH6-GFP, cotyledons of 5-day transgenic seedlings with the indicated treatments were observed under Zeiss LSM 780 confocal laser scanning microscope (CLSM) equipped with a Zeiss Alpha Plan Apochromat 63x, NA 1.40 oil objective. The mScarlet/mRuby2 and YFP/GFP signals were excited by argon lasers at 561 nm and 488 nm and collected at 495–570 nm and 570–650 nm, respectively. All the image parameters for the same transgenic lines were kept the same in this study.

Single-particle imaging and analysis of AtFH6-GFP and Lifeact-Venus-labeled actin arrays were imaged from 5-day seedlings under VA-TIRFM (Variable Angle Total Internal Reflection Fluorescence Microscope) on a Zeiss Elyra PS.1 equipped with 100×, NA 1.46 oil objective. The TIRF angle was adjusted to achieve the best SNR (signal to noise ratio). Venus and GFP signals were excited by 488-nm laser (10% laser power). For Lifeact-Venus-labeled actin array, single-frame images were captured with 1-s exposure time. For AtFH6–GFP single-particle dynamics, streaming movies were captured by the PCO. edge sCMOS camera with 100-ms exposure time for more than 90 frames.

Protein expression and purification

AtFH6-FH1COOH (FH6C) was fused with an N-terminal 6xHis tag in the pNIC-Bsa4 backbone (Ma et al., 2021). FL AtREM1.2 was fused with an N-terminal 6xHis-SUMO tag in the pSUMO-LIC backbone. The truncation variants shown in Figure 4A were generated by one-step PCR and ligation using the FL version by designing the primer pairs at the two arms of truncation points (Supplemental Table S1). AtFH1(At3G25500)-FH1COOH (FH1C) fused with N-terminal GST tag in the pGEX-4T1 backbone was reported previously (Michelot et al., 2005). All recombinant protein expression vectors were transferred to E. coli BL21 Rosetta competent cells. Positive single clones selected by appropriate antibiotics were subjected to large-scale culture in Terrific Broth medium at 37°C and 200 rpm in a New Brunswick Innova shake incubator. Induction was carried out when the bacterial optical density at 600 nm reached ~0.8 by adding 0.5-mM IPTG and further shake-incubated in 16°C for 16 h, followed by cell pelleting using JA10 rotor (Beckman Coulter) at 5,500 rpm for 15 min. The harvested cells were first resuspended in 50 mL of protein binding buffer (20-mM HEPES, pH 7.4, 500-mM NaCl, 20-mM Imidazole), supplied with one tablet of Pierce Protease Inhibitor (Thermo Scientific) and 1-mM phenylmethylsulfonyl fluoride. Cell lysis was carried out using an LM20 microfluidizer, after which the protein supernatant was collected by centrifugation using JA25.5 rotor (Beckman Coulter) at 20,000 rpm for 1 h at 4°C. The supernatant was then filtered through a 0.45-μm syringe filter and loaded onto the AKTA Xpress system (GE Healthcare). Recombinant proteins with His-tag were first enriched in

HisTrap HP columns. After washing the columns with 100-mL binding buffer, gradient elution was performed using elution buffer (20-mM HEPES, pH 7.4, 500-mM NaCl, 500-mM imidazole). Peak fractionation was conducted to collect the eluted proteins, which were further subjected to gel filtration (GF) using HiLoad 16/600 Superdex 200 pg columns and GF buffer (20-mM HEPES, pH 7.4, 300-mM NaCl, 10% [v/v] glycerol, 1-mM DTT). For AtREM1.2 recombinant proteins, SUMO digestion was carried out by adding 1/200 (molar ratio) SUMO proteinase and incubating at 4°C overnight before conducting GF. Elution peaks were collected in 1.5-mL fractions and analyzed on sodium dodecyl–sulfate polyacrylamide gel electrophoresis (SDS–PAGE) gels. The final pure proteins were concentrated using Amicon Ultra-15 Centrifugal Filter Unit to approximately 10 mg·mL^{-1} and then aliquoted into smaller fractions and stored at −80°C freezer.

Globular actin (G-actin) protein was purified from rabbit skeletal muscle by following the reported protocol (Sun et al., 2018a). Briefly, 2.5-g freeze-dry rabbit skeletal muscle power was dissolved in 200-mL G-buffer (2-mM Tris–HCl, pH 8.0, 0.2-mM CaCl$_2$, 0.2-mM ATP, 0.5-mM DTT) at 4°C for overnight, followed by centrifugation using JA25.50 rotor (Beckman Coulter) at 27,000g at 4°C for 1 h. The supernatant containing soluble actin was further polymerized by adding 2-mM MgCl$_2$ and 50-mM KCl and incubating in 4°C for 1 h. Next, 0.8-M KCl was added into the solution and incubated for 30 min to remove the actin-binding proteins. The polymerized actin filaments were further pelleted by ultracentrifugation using a Ti 55 rotor (Beckman Coulter) at 150,000g for 3 h and resuspended in 5–7 mL G-buffer, which was further subjected to dialysis in G-buffer using SnakeSkin Dialysis Tubing (Thermo Scientific) for 12 h and repeated three times. The depolymerized monomeric actin in G-buffer solution was then ultracentrifuged using Ti 55 rotor (Beckman Coulter) at 200,000g for 3 h, and the supernatant was gently collected and subjected to gel filtration chromatography using HiPrep 16/60 Sephacryl S-300 HR column (GE Healthcare). The final collected actin purity was verified on an SDS–PAGE gel.

Protein labeling

To carry out fluorescent labeling of the recombinant proteins, 10-μL Alexa Fluor 488/647 NHS Ester (Invitrogen) (0.5 mg·mL^{-1} stock in DMSO) was mixed with 2-mg protein solution (concentration >2 mg·mL^{-1}) supplied with 0.1-M NaHCO$_3$, and incubated for 1 h at room temperature or overnight at 4°C. The labeled proteins were further purified by HiTrap Desalting column (GE Healthcare) with protein buffer (20-mM HEPES, pH 7.4, 300-mM NaCl) to remove the free dye. To label the G-actin with Oregon Green (488) and Biotin Oregon Green 488 iodoacetamide (ThermoFisher) and NHS-dPEG4-biotin (Sigma) were dissolved in DMSO to generate a 10-mM stock. The purified G-actin was first diluted in chilled 2× labeling buffer (50-mM imidazole, pH 7.4, 200-mM KCl, 0.3-mM ATP, 4-mM MgCl$_2$) to a final concentration of 23 μM. Then, the dye stocks were added to

the buffer as a 15-fold molar excess of actin. The mixture was covered with aluminum foil and gently rotated in the dark at 4°C overnight, during which monomeric actin was polymerized to actin filaments. Afterward, the actin filaments were depolymerized and purified following the same protocol for G-actin purification as described above.

Protein size calibration

Calibration standard proteins (Sigma-Aldrich): Bovine serum albumin (66 kDa), alcohol dehydrogenase (150 kDa), β-Amylase (200 kDa), apoferritin (443 kDa), carbonic anhydrase (29 kDa), thyroglobulin (669 kDa), were dissolved in calibration buffer (20-mM HEPES, pH 7.4, 150-mM NaCl, 1-mM DTT) to 10 mg·mL^{-1} as stock concentrations. The Superdex 200 Increase 10/300 GL (GE Healthcare) column was first balanced by calibration buffer using AKTA Xpress system). Then 10 μL of each calibration standard protein was mixed and subjected to SEC with the same calibration buffer. The target proteins were further calibrated by loading ∼100 ng proteins into the same column and using the same calibration buffer for SEC. The target protein size was defined by comparing the elution volume of the target proteins with standard proteins.

Actin assembly assay in vitro

The pyrene–actin assembly assay was conducted by following the published protocol (Sun et al., 2018a). Briefly, a 10-μM Mg^{2+}–ATP–actin mix was first prepared by mixing 9.7-mM rabbit G-actin (described above) and 0.3-mM pyrene-labeled actin (Cytoskeleton Inc.) was first mixed in G-buffer supplied with 200-mM EGTA and 110-mM MgCl$_2$ to prepare a 10-μM Mg^{2+}–ATP–actin mix. Then, actin polymerization was initiated by adding 12-μL KME mixture (500-mM KCl, 10-mM MgCl$_2$, and 10-mM EGTA) and 25-μL Mg^{2+}–ATP–actin mix into 83-μL G-buffer containing with or without other proteins. The pyrene fluorescence signal was excited using a Xenon Flash lamp at 365 nm, and the emission was collected at 407 nm at 25°C with 15-s intervals using a BioTek Cytation 5 cell imaging multimode reader. The actin polymerization rate was quantified by comparing the linear increase rates using fluorescence values in between 0 s and 100–500 s after actin polymerization that had a R^2 value greater than 0.95. The slope was recorded as the polymerization rate for each reaction.

Real-time monitoring of actin assembly was performed on biotin-coated glass slices and captured under TIRFM. To coat the glass slice, 24 × 50 mm, No 1.5 microscope cover glasses (Paul Marienfeld) were immersed in 20% sulfuric acid overnight, followed by thorough rinsing with distilled water. The glasses were then immersed in 80% ethanol (pH 2.0) supplied with 2 mg·mL^{-1} methoxy-PEG-silane and 2 μg·mL^{-1} biotin-PEG-silane (Laysan Bio Inc.) overnight at 70°C. After washing with distilled water and drying under N$_2$ gas, the glasses were stored at −80°C and were attached to six-cell chamber slices (Ibidi) before actin assembly was performed following a published method (Jansen and Goode, 2019). Briefly, the chamber was first blocked by 30-μL HBSA buffer

(20-mM HEPES, pH 7.4, 1-mM EDTA, 50-mM KCl, 1% [m/v] BSA) for 30 s, followed with streptavidin conjugation by adding 30-μL HEKG10 buffer (20-mM HEPES, pH 7.4, 1-mM EDTA, 50-mM KCl, 10% [v/v] glycerol, 0.1 mg·mL^{-1} streptavidin) for 1 min. 1 × TIRFM buffer (10-mM imidazole, pH 7.4, 50-mM KCl, 1-mM MgCl$_2$, 1-mM EGTA, 50-mM DTT, 0.3-mM ATP, 20-nM CaCl$_2$, 15-mM glucose, 100-μg·mL^{-1} glucose oxidase, 15 μg·mL^{-1} catalase, 0.25% methylcellulose) was then used to wash the chamber six times before actin polymerization on the glasses by adding 30-μL 2 × TIRFM buffer plus 30-μL actin mix containing 1.5-μM actin (89.5% G-actin, 10% Oregon Green 488-actin, 0.5% biotin–actin), 200-mM EGTA, 110-mM MgCl$_2$ supplied with or without indicated proteins. The Oregon green-actin signal was excited with a 495-nm laser and captured by Nikon ECLIPSE Ti-S inverted microscope equipped with an Apochromat 100×, NA 1.49, objective and Evolve 512 EMCCD camera with 5 s interval for more than 10 min.

Fluorescence anisotropy assay

To determine the direct interaction of FH1C/FH6C and REM variants and measure the binding affinity, 90-nM Alexa Fluor 647-labeled FH1C/FH6C (as described above) was first mixed with serial 2 × diluted REM (ligands) from 32 μM to 1 nM to a final volume of 30 μL in each well of 384-well flat bottom plate (Greiner Bio-One) and incubated at 4°C for 20 min. The fluorescence signal at parallel (I_{pa}) and perpendicular (I_{per}) directions was measured with a Spark multimode plate reader (TECAN) using fluorescence polarization mode (excitation filter: 638 nm, 20 nm bandpass; emission filter: 684 nm, 20 nm bandpass). The fluorescence anisotropy (r) was further calculated following the equation: $r = (I_{pa} - I_{per})/(I_{pa} + 2I_{per})$ and normalized by the r of 90-nM Alexa Fluor 647-labeled FH1C/FH6C alone. The normalized fluorescence anisotropy was fitted using the Hill slope equation in GraphPad Prism 6 with the means from at least three independent experiments to calculate the binding affinity.

Lipid membrane reconstitution

1-Palmitoyl-2-oleoyl-glycero-3-phosphocholine (POPC), 1,2-dioleoyl-sn-glycero-3-[(N-(5-amino-1-carboxypentyl) iminodiacetic acid) succinyl] (nickel salt, DGS-NTA-Ni), 1,2-dioleoyl-sn-glycero-3-phosphoethanolamine-N-[4-(p-maleimido-methyl) cyclohexane-carboxamide] (MCC-PE) were purchased from Avanti Polar Lipids. To prepare the Small Unilamellar Vesicles (SUVs), the lipid mixture (88% POPC, 10% DGS-NTA-Ni, 2% MCC-PE) was first incubated in 40°C water for 10 min with gentle shaking and then dried under N$_2$ gas until all the chloroform was evaporated, followed by further drying for 2 h using a vacuum pump. Rehydration was then performed by adding PBS buffer (pH 7.4) to a final concentration of 1 mg·mL^{-1} and sonication in the water bath for 30 min. Subsequently, freeze–thaw cycles were applied to lipid vesicles using liquid N$_2$ and a 42°C water bath for 20 cycles. Finally, the SUVs were formed by extruding the lipid vesicles through a 100-nm polycarbonate filter membrane (Avanti Polar Lipids) 20 times. The SLBs were

formed in a 96-well glass-bottom plate, which was cleaned by Hellmanex III (Sigma Aldric) overnight and further cleaned using 5-M NaOH for 3 h before adding 50-µL SUVs containing 0.5–1 mg·mL^{-1} lipids in each well. The plate was then incubated at 37°C for 30 min to form SLBs and washed with PBS six times to remove the free vesicle. PBS (50 µL) was retained in the well to avoid lipid oxidation during each wash and the subsequent buffer exchange.

To reconstitute the protein interaction on lipid membrane, the SLBs were first blocked by adding 300-µL PBS containing 2 mg·mL^{-1} casein (Sigma Aldrich) into the well and incubating for 10 min. Subsequently, the PBS was washed away by protein buffer (50-mM HEPES, pH 7.4, 150-mM NaCl, 1-mM TCEP) for six times. Then, 30-nM FH1C/FH6C (10% Alexa 647-FH1C) was premixed with or without REM (10% Alexa 488-REM) FL or truncating protein variants with the indicated molar ratios in protein buffer and incubated for 2 min, and further added to the well. After 1 min of conjugation, the free proteins in the solution were rinsed away with protein buffer. Then the SLBs conjugated with proteins were imaged using Nikon ECLIPSE Ti-S TIRFM as described above.

Bacterial population quantification

To quantify the internal bacterial population, three to four individual seedlings in each plate were collected and weighed each day post inoculation. The seedlings were surface sterilized in 70% ethanol for 10 s and further washed twice in autoclaved distilled water for 20 s. Each individual seedling was then homogenized using PowerLyzer 24 (QIAGEN) and resuspended in 200 µL of 10-mM MgCl$_2$. The homogenized suspension was subjected to 10× serial dilution eight times, plated on the NYG plate, and cultured in a 30°C incubator for 2 days. The bacterial CFU was further counted and normalized by the weight of each seedling.

Fluorescent-tagged protein clustering and dynamic analysis

To quantify the YFP-AtREM1.2/AtREM1.3 and AtFH6-GFP punctate foci signal total intensity. The CLSM recorded single frame images were duplicated in ImageJ and converted to stacks. After background subtraction, the Trackmate plugin was used to track the YFP-AtREM1.2/AtREM1.3 and AtFH6-GFP punctate particles in each frame. Based on manually preliminary particle analysis in ImageJ, the estimated particle diameter was set to 0.5 µm and 0.4 µm for YFP-AtREM1.2/AtREM1.3 and AtFH6-GFP, respectively, for particle detection. Quality control was additionally carried out by filtering out false selection from the background until only visible punctate protein signals were selected. Unless specific conditions, such as extremely weak particle signals, the quality was set as the same value for each image to ensure unbiased particle selection. The selected particles were further subjected to signal intensity analysis in Trackmate. More than 200 particles from at least ten images were quantified for each Arabidopsis line. Single particle intensity analysis for Alexa 647-FH1C, Alexa 647-FH6C on SLB was also conducted

using the same approach as described above. As AtFH2-eGFP forms more diffused signal on PM under CLSM, selecting each individual AtFH2-eGFP puncta is not practicle. We thus analyzed the SCI of AtFH2-eGFP, which is another well-defined parameter to indicate the molecular clustering (Gronnier et al., 2017; Tran et al., 2020). The SCI was analyzed by measuring the ratio of the mean signal intensity of the top 5% of pixels with the highest intensity and 5% of pixels with the lowest intensity in each region of interest (ROI; a line 10 µm in length; Gronnier et al., 2017). Sixty ROIs from more than ten images were quantified for each treatment.

To analyze the colocalization of mRuby2/mScarlet-AtREM1.2 and AtFH6-GFP, the two-channel images were first cropped into 20 µm × 20 µm sized ROIs that were well focused, followed by applying the background substation function of ImageJ by setting the rolling ball radius as 50 pixels to channel. Then the images were further subjected to Pearson correlation coefficient quantification through ImageJ plugin coloc 2 by setting default parameters. More than 30 ROIs were quantified for each treatment. To quantify the association ratio of mRuby2-AtREM1.2 particles on F-actin, the two-channel images were first cropped into 20 µm × 20 µm sized ROIs, the association ratio was analyzed by counting the numbers of mRuby2-AtREM1.2 particles, which localize on top or directly associate at the side of the F-actin (with or without F-actin image rotated by 90°), divided by the total mRuby2-AtREM1.2 particle numbers. More than 30 ROIs from at least 10 images were quantified for each treatment.

Single-particle dynamic analysis of AtFH6-GFP was conducted using SpatTrack. The time-lapse images were first cropped into 5 µm × 5 µm sized ROIs, which were evenly illuminated. Based on manual preliminary measurement in ImageJ, the estimated particle diameter was set to 0.35 µm for denoising and particle detection. An identical threshold range was further applied on each ROI to precisely detect all the particles, after which a maximum displacement in each frame was set as 0.5 µm to track the particle trajectories over time. Only trajectories with more than 15 frames were subjected to MSD and diffusion coefficient quantification using the anomalous diffusion analytical model described previously (Ma et al., 2021). More than 30 cropped time-lapse images were analyzed in each treatment with the same parameters.

Actin array architecture analysis

Actin array quantification was analyzed by using the "Skewness" and "Density" scripts (http://daylab.plp.msu.edu/wp-content/uploads) in ImageJ (Higaki et al., 2010; Lu and Day, 2017). The VA-TIRFM recorded actin images were first cropped into ROIs based on the principle that each ROI should contain the largest in-focus area of one cell. For F-actin density quantification, the identical threshold range was first applied to each ROI to select F-actin before being subjected to ImageJ "Density" script to quantify F-actin occupied pixel numbers. The F-actin occupancy was calculated

by normalizing the filament-occupied pixel area by the ROI area (%). To analyze actin bundling, "Skewness" script was used to calculate the skewness of F-actin's fluorescence intensity distribution, which is higher when the filaments are more bundled as the intensity distribution becomes more skewed (Higaki et al., 2010). For each treatment, more than 25 cropped ROIs from at least 10 images were quantified to analyze the actin array architecture.

To quantify the actin seed number in TIRFM, actin assembly was recorded in vitro. The image frame at the indicated time points was cropped into 20 μm × 20 μm ROIs to quantify the actin seed number. The seed number in each ROI was manually counted in ImageJ from at least 10 ROIs for each treatment condition or time point.

Statistical analysis

For all the cell biology imaging, at least two biological replications were conducted, and more than three seedlings were imaged in each replication. Image quantification was conducted in multiple cells or ROIs (as described in figure legends) from at least 10-well-focused images for each condition. Statistical analyses were performed in Prism 6.0 (GraphPad). Comparisons between two groups were conducted using a two-tailed Student's t test assuming equal variances, while multiple comparisons between more than three groups were carried out using one-way ANOVA. *$P \leqslant 0.05$; **$P \leqslant 0.01$; ***$P \leqslant 0.001$; ****$P \leqslant 0.0001$, ns = not significant. Unless specified, the data were plotted as bar graphs with error bars = SD, or boxplots, in which the square boxes indicate the 25% and 75% quartiles with median inside, and "+" indicates the mean value. Source data and information on the statistical analysis are provided in Supplemental Data Set S1.

Accession numbers

Accession numbers of genes reported in this study are listed as follows: *AtFH6*, AT5G67470; *AtFH2*, AT2G43800; *AtFH1*, At3G25500; *AtREM1.2*, AT3G61260; *AtREM1.3*, AT2G45820.

Supplemental data

The following materials are available in the online version of this article.

Supplemental Figure S1. Formin and remorin clustering in Arabidopsis PTI responses. Supports Figure 1.

Supplemental Figure S2. Perturbation of lipid nanodomain assembly impairs PAMP-triggered formin clustering and actin polymerization under PTI signaling. Supports Figure 1.

Supplemental Figure S3. Characterization of remorin clustering in the presence of multiple PAMPs and Arabidopsis PTI responses in actin assembly-deficient conditions. Supports Figure 1 and 2.

Supplemental Figure S4. Overexpression of remorin condenses and stabilizes formin. Supports Figure 2.

Supplemental Figure S5. In vitro reconstitution of formin and remorin on the lipid membrane. Supports Figure 3.

Supplemental Figure S6. The IDR and CC domain of AtREM1.2 promote AtREM1.2 mediated formin clustering. Supports Figure 4.

Supplemental Table S1. Sequences of primers used in this study.

Supplemental Data Set S1. Source data and statistical analysis.

Supplemental Movie S1. Perturbation of lipid nanodomain assembly impairs PAMP-triggered formin stabilization.

Supplemental Movie S2. Overexpression of remorin stabilizes formin on plasma membrane.

References

Abel NB, Buschle CA, Hernandez-Ryes C, Burkart SS, Deroubaix A-F, Mergner J, Gronnier J, Jarsch IK, Folgmann J, Braun KH (2021) A hetero-oligomeric remorin-receptor complex regulates plant development. bioRxiv. DOI: 10.1101/2021.01.28.428596 [Posted on January 29, 2021]

Alberti S, Halfmann R, King O, Kapila A, Lindquist S (2009) A systematic survey identifies prions and illuminates sequence features of prionogenic proteins. Cell **137:** 146–158

Banani SF, Lee HO, Hyman AA, Rosen MK (2017) Biomolecular condensates: organizers of cellular biochemistry. Nat Rev Mol Cell Biol **18:** 285–298

Bariola P, Retelska D, Stasiak A, Kammerer R, Fleming A, Hijri M, Frank S, Farmer E (2004) Remorins form a novel family of coiled coil-forming oligomeric and filamentous proteins associated with apical, vascular and embryonic tissues in plants. Plant Mol Biol **55:** 579–594

Brühmann S, Ushakov DS, Winterhoff M, Dickinson RB, Curth U, Faix J (2017) Distinct VASP tetramers synergize in the processive elongation of individual actin filaments from clustered arrays. Proc Natl Acad Sci USA **114:** E5815–E5824

Bücherl CA, Jarsch IK, Schudoma C, Segonzac C, Mbengue M, Robatzek S, MacLean D, Ott T, Zipfel C (2017) Plant immune and growth receptors share common signalling components but localise to distinct plasma membrane nanodomains. eLife 6: e25114

Buttery SM, Yoshida S, Pellman D (2007) Yeast formins Bni1 and Bnr1 utilize different modes of cortical interaction during the assembly of actin cables. Mol Biol Cell 18: 1826–1838

Case LB, Ditlev JA, Rosen MK (2019a) Regulation of transmembrane signaling by phase separation. Annu Rev Biophys 48: 465–494

Case LB, Zhang X, Ditlev JA, Rosen MK (2019b) Stoichiometry controls activity of phase-separated clusters of actin signaling proteins. Science 363: 1093–1097

Choi J-M, Pappu RV (2020) The stickers and spacers framework for describing phase behavior of multivalent intrinsically disordered proteins. Biophys J 118: 492a

Damme DV, Bouget FY, Poucke KV, Inzé D, Geelen D (2004) Molecular dissection of plant cytokinesis and phragmoplast structure: a survey of GFP-tagged proteins. Plant J 40: 386–398

Deeks MJ, Hussey PJ, Davies B (2002) Formins: intermediates in signal-transduction cascades that affect cytoskeletal reorganization. Trends Plant Sci 7: 492–498

Diao M, Ren S, Wang Q, Qian L, Shen J, Liu Y, Huang S (2018) Arabidopsis formin 2 regulates cell-to-cell trafficking by capping and stabilizing actin filaments at plasmodesmata. eLife 7: e36316

Diaz-Rohrer BB, Leventa KR, Simons K, Levental I (2014) Membrane raft association is a determinant of plasma membrane localization. Proc Natl Acad Sci USA 111: 8500–8505

Emenecker RJ, Holehouse AS, Strader LC (2020) Emerging roles for phase separation in plants. Dev Cell 55: 69–83

Era A, Tominaga M, Ebine K, Awai C, Saito C, Ishizaki K, Yamato KT, Kohchi T, Nakano A, Ueda T (2009) Application of Lifeact reveals F-actin dynamics in Arabidopsis thaliana and the liverwort, Marchantia polymorpha. Plant Cell Physiol 50: 1041–1048

Errington WJ, Bruncsics B, Sarkar CA (2019) Mechanisms of noncanonical binding dynamics in multivalent protein–protein interactions. Proc Natl Acad Sci USA 116: 25659–25667

Favery B, Chelysheva LA, Lebris M, Jammes F, Marmagne A, De Almeida-Engler J, Lecomte P, Vaury C, Arkowitz RA, Abad P (2004) Arabidopsis formin AtFH6 is a plasma membrane-associated protein upregulated in giant cells induced by parasitic nematodes. Plant Cell 16: 2529–2540

Feng Z, Chen X, Wu X, Zhang M (2019a) Formation of biological condensates via phase separation: Characteristics, analytical methods, and physiological implications. J Biol Chem 294: 14823–14835

Feng Z, Chen X, Zeng M, Zhang M (2019b) Phase separation as a mechanism for assembling dynamic postsynaptic density signalling complexes. Curr Opin Neurobiol 57: 1–8

Garcia-Parajo MF, Cambi A, Torreno-Pina JA, Thompson N, Jacobson K (2014) Nanoclustering as a dominant feature of plasma membrane organization. J Cell Sci 127: 4995–5005

Gouguet P, Gronnier J, Legrand A, Perraki A, Jolivet M-D, Deroubaix A-F, German-Retana S, Boudsocq M, Habenstein B, Mongrand S, et al. (2021) Connecting the dots: from nanodomains to physiological functions of REMORINs. Plant Physiol 185: 632–649

Gowrishankar K, Ghosh S, Saha S, Rumamol C, Mayor S, Rao M (2012) Active remodeling of cortical actin regulates spatiotemporal organization of cell surface molecules. Cell 149: 1353–1367

Gronnier J, Crowet J-M, Habenstein B, Nasir MN, Bayle V, Hosy E, Platre MP, Gouguet P, Raffaele S, Martinez D (2017) Structural basis for plant plasma membrane protein dynamics and organization into functional nanodomains. eLife 6: e26404

Haynes C, Oldfield CJ, Ji F, Klitgord N, Cusick ME, Radivojac P, Uversky VN, Vidal M, Iakoucheva LM (2006) Intrinsic disorder is a common feature of hub proteins from four eukaryotic interactomes. PLOS Comput Biol 2: e100

Henty-Ridilla JL, Li J, Day B, Staiger CJ (2014) ACTIN DEPOLYMERIZING FACTOR4 regulates actin dynamics during innate immune signaling in Arabidopsis. Plant Cell 26: 340–352

Henty-Ridilla JL, Shimono M, Li J, Chang JH, Day B, Staiger CJ (2013) The plant actin cytoskeleton responds to signals from microbe-associated molecular patterns. PLoS Pathog 9: e1003290

Hetrick B, Han MS, Helgeson LA, Nolen BJ (2013) Small molecules CK-666 and CK-869 inhibit actin-related protein 2/3 complex by blocking an activating conformational change. Chem Biol 20: 701–712

Higaki T, Kutsuna N, Sano T, Kondo N, Hasezawa S (2010) Quantification and cluster analysis of actin cytoskeletal structures in plant cells: role of actin bundling in stomatal movement during diurnal cycles in Arabidopsis guard cells. Plant J 61: 156–165

Hind SR, Strickler SR, Boyle PC, Dunham DM, Bao Z, O'Doherty IM, Baccile JA, Hoki JS, Viox EG, Clarke CR, et al. (2016) Tomato receptor FLAGELLIN-SENSING 3 binds flgII-28 and activates the plant immune system. Nat Plants 2: 16128

Huang D, Sun Y, Ma Z, Ke M, Cui Y, Chen Z, Chen C, Ji C, Tran TM, Yang L (2019) Salicylic acid-mediated plasmodesmal closure via Remorin-dependent lipid organization. Proc Natl Acad Sci USA 116: 21274–21284

Ishiga Y, Ishiga T, Uppalapati SR, Mysore KS (2011) Arabidopsis seedling flood-inoculation technique: a rapid and reliable assay for studying plant-bacterial interactions. Plant Methods 7: 32

Jaillais Y, Ott T (2020) The nanoscale organization of the plasma membrane and its importance in signaling: a proteolipid perspective. Plant Physiol 182: 1682–1696

Jansen S, Goode BL (2019) Tropomyosin isoforms differentially tune actin filament length and disassembly. Mol Biol Cell 30: 671–679

Jarsch IK, Konrad SS, Stratil TF, Urbanus SL, Szymanski W, Braun P, Braun K-H, Ott T (2014) Plasma membranes are subcompartmentalized into a plethora of coexisting and diverse microdomains in Arabidopsis and Nicotiana benthamiana. Plant Cell 26: 1698–1711

Kalappurakkal JM, Sil P, Mayor S (2020) Toward a new picture of the living plasma membrane. Protein Sci 29: 1355–1365

Kastritis PL, Bonvin AMJJ (2013) On the binding affinity of macromolecular interactions: daring to ask why proteins interact. J R Soc Interface 10: 20120835

Ke M, Ma Z, Wang D, Sun Y, Wen C, Huang D, Chen Z, Yang L, Tan S, Li R (2020) Salicylic acid regulates PIN2 auxin transporter hyperclustering and root gravitropic growth via Remorin-dependent lipid nanodomain organisation in Arabidopsis thaliana. New Phytol. DOI: 10.1111/nph.16915

Keinath NF, Kierszniowska S, Lorek J, Bourdais G, Kessler SA, Shimosato-Asano H, Grossniklaus U, Schulze WX, Robatzek S, Panstruga R (2010) PAMP (pathogen-associated molecular pattern)-induced changes in plasma membrane compartmentalization reveal novel components of plant immunity. J Biol Chem 285: 39140–39149

King MR, Petry S (2020) Phase separation of TPX2 enhances and spatially coordinates microtubule nucleation. Nat Commun 11: 1–13

Kusumi A, Shirai YM, Koyama-Honda I, Suzuki KGN, Fujiwara TK (2010) Hierarchical organization of the plasma membrane: investigations by single-molecule tracking vs. fluorescence correlation spectroscopy. FEBS Lett 584: 1814–1823

Legrand A, Martinez D, Grélard A, Berbon M, Morvan E, Tawani A, Loquet A, Mongrand S, Habenstein B (2019) Nanodomain clustering of the plant protein Remorin by solid-state NMR. Front Mol Biosci 6: 107

Li J, Henty-Ridilla JL, Staiger BH, Day B, Staiger CJ (2015) Capping protein integrates multiple MAMP signalling pathways to modulate actin dynamics during plant innate immunity. Nat Commun 6: 7206

Li J, Staiger CJ (2018) Understanding cytoskeletal dynamics during the plant immune response. Annu Rev Phytopathol 56: 513–533

Li P, Day B (2019) Battlefield cytoskeleton: turning the tide on plant immunity. Mol Plant-Microbe Interact 32: 25–34

Liang P, Stratil TF, Popp C, Marín M, Folgmann J, Mysore KS, Wen J, Ott T (2018) Symbiotic root infections in Medicago truncatula require remorin-mediated receptor stabilization in membrane nanodomains. Proc Natl Acad Sci USA 115: 5289–5294

López CA, de Vries AH, Marrink SJ (2011) Molecular mechanism of cyclodextrin mediated cholesterol extraction. PLoS Comput Biol 7: e1002020

Lu Y-J, Day B (2017) Quantitative evaluation of plant actin cytoskeletal organization during immune signaling. Methods Mol Biol 1578: 207–221

Luna E, Pastor V, Robert J, Flors V, Mauch-Mani B, Ton J (2011) Callose deposition: a multifaceted plant defense response. Mol Plant-Microbe Interact 24: 183–193

Ma Z, Liu X, Nath S, Sun H, Tran TM, Yang L, Mayor S, Miao Y (2021) Formin nanoclustering-mediated actin assembly during plant flagellin and DSF signaling. Cell Rep 34: 108884

Marin M, Ott T (2012) Phosphorylation of intrinsically disordered regions in remorin proteins. Front Plant Sci 3: 86

Marin M, Thallmair V, Ott T (2012) The intrinsically disordered N-terminal region of AtREM1.3 remorin protein mediates protein-protein interactions. J Biol Chem 287: 39982–39991

Marín M, Thallmair V, Ott T (2012) The intrinsically disordered N-terminal region of AtREM1. 3 remorin protein mediates protein-protein interactions. J Biol Chem 287: 39982–39991

Martinez D, Legrand A, Gronnier J, Decossas M, Gouguet P, Lambert O, Berbon M, Verron L, Grélard A, Germain V (2019) Coiled-coil oligomerization controls localization of the plasma membrane REMORINs. J Struct Biol 206: 12–19

Martiniere A, Gayral P, Hawes C, Runions J (2011) Building bridges: formin1 of Arabidopsis forms a connection between the cell wall and the actin cytoskeleton. Plant J 66: 354–365

Miao Y, Tipakornsaowapak T, Zheng L, Mu Y, Lewellyn E (2018) Phospho-regulation of intrinsically disordered proteins for actin assembly and endocytosis. FEBS J 285: 2762–2784

Michelot A, Derivery E, Paterski-Boujemaa R, Guérin C, Huang S, Parcy F, Staiger CJ, Blanchoin L (2006) A novel mechanism for the formation of actin-filament bundles by a nonprocessive formin. Curr Biol 16: 1924–1930

Michelot A, Guérin C, Huang S, Ingouff M, Richard S, Rodiuc N, Staiger CJ, Blanchoin L (2005) The formin homology 1 domain modulates the actin nucleation and bundling activity of Arabidopsis FORMIN1. Plant Cell 17: 2296–2313

Mostowy S, Shenoy AR (2015) The cytoskeleton in cell-autonomous immunity: structural determinants of host defence. Nat Rev Immunol 15: 559–573

Ojosnegros S, Cutrale F, Rodríguez D, Otterstrom JJ, Chiu CL, Hortigüela V, Tarantino C, Seriola A, Mieruszynski S, Martínez E (2017) Eph-ephrin signaling modulated by polymerization and condensation of receptors. Proc Natl Acad Sci USA 114: 13188–13193

Perraki A, Cacas JL, Crowet JM, Lins L, Castroviejo M, German-Retana S, Mongrand S, Raffaele S (2012) Plasma membrane localization of Solanum tuberosum remorin from group 1, homolog 3 is mediated by conformational changes in a novel C-terminal anchor and required for the restriction of potato virus X movement]. Plant Physiol 160: 624–637

Perraki A, Gronnier J, Gouguet P, Boudsocq M, Deroubaix A-F, Simon V, German-Retana S, Zipfel C, Bayer E, Mongrand S (2018) REM1. 3's phospho-status defines its plasma membrane nanodomain organization and activity in restricting PVX cell-to-cell movement. PLoS Pathogens 14: e1007378

Raffaele S, Bayer E, Lafarge D, Cluzet S, Retana SG, Boubekeur T, Leborgne-Castel N, Carde J-P, Lherminier J, Noirot E (2009) Remorin, a solanaceae protein resident in membrane rafts and plasmodesmata, impairs potato virus X movement. Plant Cell 21: 1541–1555

Saha S, Lee IH, Polley A, Groves JT, Rao M, Mayor S (2015) Diffusion of GPI-anchored proteins is influenced by the activity of dynamic cortical actin. Mol Biol Cell 26: 4033–4045

Sezgin E, Levental I, Mayor S, Eggeling C (2017) The mystery of membrane organization: composition, regulation and roles of lipid rafts. Nat Rev Mol Cell Biol 18: 361

Sil P, Mateos N, Nath S, Buschow S, Manzo C, Suzuki KG, Fujiwara T, Kusumi A, Garcia-Parajo MF, Mayor S (2020) Dynamic actin-mediated nano-scale clustering of CD44 regulates its meso-scale organization at the plasma membrane. Mol Biol Cell 31: 561–579

Staiger CJ, Sheahan MB, Khurana P, Wang X, McCurdy DW, Blanchoin L (2009) Actin filament dynamics are dominated by rapid growth and severing activity in the Arabidopsis cortical array. J Cell Biol 184: 269–280

Stone MB, Shelby SA, Núñez MF, Wisser K, Veatch SL (2017) Protein sorting by lipid phase-like domains supports emergent signaling function in B lymphocyte plasma membranes. eLife 6: e19891

Su X, Ditlev JA, Hui E, Xing W, Banjade S, Okrut J, King DS, Taunton J, Rosen MK, Vale RD (2016) Phase separation of signaling molecules promotes T cell receptor signal transduction. Science 352: 595–599

Sun H, Luo Y, Miao Y (2018a) Purification of globular actin from rabbit muscle and pyrene fluorescent assays to investigate actin dynamics in vitro. Bio-protocol 8: e3102

Sun H, Qiao Z, Chua KP, Tursic A, Liu X, Gao YG, Mu Y, Hou X, Miao Y (2018b. Profilin negatively regulates formin-mediated actin assembly to modulate PAMP-triggered plant immunity. Curr Biol 28: 1882–1895 e1887

Sun H, Zhu X, Li C, Ma Z, Han X, Luo Y, Yang L, Yu J, Miao Y (2021) Xanthomonas effector XopR hijacks host actin cytoskeleton via complex coacervation. Nat Commun 12: 4064

Tran TM, Ma Z, Triebl A, Nath S, Cheng Y, Gong B-Q, Han X, Wang J, Li J-F, Wenk MR, et al. (2020) The bacterial quorum sensing signal DSF hijacks Arabidopsis thaliana sterol biosynthesis to suppress plant innate immunity. Life Sci Alliance 3: e202000720

Wang J, Choi JM, Holehouse AS, Lee HO, Zhang X, Jahnel M, Maharana S, Lemaitre R, Pozniakovsky A, Drechsel D, et al. (2018) A molecular grammar governing the driving forces for phase separation of prion-like RNA binding proteins. Cell 174: 688–699.16

Woodruff JB, Ferreira Gomes B, Widlund PO, Mahamid J, Honigmann A, Hyman AA (2017) The centrosome is a selective condensate that nucleates microtubules by concentrating tubulin. Cell 169: 1066–1077.e10.

Wright PE, Dyson HJ (2015) Intrinsically disordered proteins in cellular signalling and regulation. Nat Rev Mol Cell Biol 16: 18–29

Wu X, Cai Q, Feng Z, Zhang M (2020) Liquid-liquid phase separation in neuronal development and synaptic signaling. Dev Cell 55: 18–29

Xiao Q, McAtee CK, Su X (2021) Phase separation in immune signalling. Nat Rev Immunol https://doi.org/10.1038/s41577-021-00572-5

Xie Y, Loh ZY, Xue J, Zhou F, Sun J, Qiao Z, Jin S, Deng Y, Li H, Wang Y, et al. (2020) Orchestrated actin nucleation by the Candida albicans polarisome complex enables filamentous growth. J Biol Chem 295: 14840–14854

Xie Y, Miao Y (2021) Polarisome assembly mediates actin remodeling during polarized yeast and fungal growth. J Cell Sci **134**: jcs247916

Xie Y, Sun J, Han X, Tursic-Wunder A, Toh JDW, Hong W, Gao YG, Miao Y (2019) Polarisome scaffolder Spa2-mediated macromolecular condensation of Aip5 for actin polymerization. Nat Commun **10**: 5078

Zeng M, Chen X, Guan D, Xu J, Wu H, Tong P, Zhang M (2018) Reconstituted postsynaptic density as a molecular platform for understanding synapse formation and plasticity. Cell **174**: 1172–1187.16.

Zhao YG, Zhang H (2020) Phase separation in membrane biology: the interplay between membrane-bound organelles and membraneless condensates. Dev Cell **55**: 30–44